Numeričko modeliranje procesa izgaranja u komori za izgaranje mlaznog motora korištenjem kemijske kinetike i pristupa tabeliranih podataka propagacije plamena

Pađen, Ivan

Master's thesis / Diplomski rad

2018

Degree Grantor / Ustanova koja je dodijelila akademski / stručni stupanj: **University of Zagreb, Faculty of Mechanical Engineering and Naval Architecture / Sveučilište u Zagrebu, Fakultet strojarstva i brodogradnje**

Permanent link / Trajna poveznica: https://urn.nsk.hr/urn:nbn:hr:235:615905

Rights / Prava: In copyright/Zaštićeno autorskim pravom.

Download date / Datum preuzimanja: **2025-04-03**

Repository / Repozitorij:

Repository of Faculty of Mechanical Engineering and Naval Architecture University of Zagreb

UNIVERSITY OF ZAGREB

FACULTY OF MECHANICAL ENGINEERING AND NAVAL ARCHITECTURE

MASTER'S THESIS

Ivan Pađen

ZAGREB, 2018.

University of Zagreb

Faculty of Mechanical Engineering and Naval Architecture

Master's Thesis

Numerical Modelling of the Combustion Process in a Jet

Engine Combustion Chamber Using the Chemical Kinetics

and Flamelet Gnerated Manifold Approaches

Mentor: Student:

Asst. prof. dr. sc. Milan Vujanović   Ivan Pađen

Zagreb, 2018.

Sveučilište u Zagrebu	
Fakultet strojarstva i brodogradnje	
Datum	Prilog
Klasa:	
Ur.broj:	

DIPLOMSKI ZADATAK

Student: **Ivan Pađen** Mat. br.: 0035186213

Naslov rada na hrvatskom jeziku: **Numeričko modeliranje procesa izgaranja u komori za izgaranje mlaznog motora korištenjem kemijske kinetike i pristupa tabeliranih podataka propagacije plamena**

Naslov rada na engleskom jeziku: **Numerical Modelling of the Combustion Process in a Jet Engine Combustion Chamber Using the Chemical Kinetics and Flamelet Generated Manifold Approaches**

Opis zadatka:

Korištenje računalne dinamike fluida (RDF) u kombinaciji s eksperimentalnim pristupom postao je uobičajen pristup u razvoju različitih inženjerskih sustava. Uslijed utjecaja inercije, površinske napetosti i aerodinamičkih sila dolazi do raspadanja goriva na sitne kapljice, njihovog isparavanja te miješanja sa smjesom plinova. Prilikom rada mlaznog motora, unutar komore za izgaranje dolazi do stvaranja spreja i miješanja goriva sa zrakom te do procesa zapaljenja. U okviru diplomskog zadatka potrebno je:

1. Opisati osnovne jednadžbe računalne dinamike fluida te opisati jednadžbe korištene za opisivanje procesa spreja i procesa izgaranja;
2. Opisati jednadžbe modeliranja kemijske kinetike i pristupa tabeliranih podataka propagacije plamena za opisivanje procesa izgaranja;
3. Prikazati numeričke postavke koje će se koristiti za rješavanje problema;
4. Računalno modelirati proces ubrizgavanja i proces izgaranja u komori mlaznog motora;
5. Obrazložiti izračunate rezultate.

Sva potrebna literatura, opis modela te ulazni i početni podaci za analizu slučaja bit će dostupni od strane mentora.

U radu je potrebno navesti korištenu literaturu i eventualno dobivenu pomoć.

Zadatak zadan: Rok predaje rada: Predviđeni datumi obrane:

18. siječnja 2018.   22. ožujka 2018.   28., 29. i 30. ožujka 2018.

Zadatak zadao: Predsjednik Povjerenstva:

Doc. dr. sc. Milan Vujanović   Prof. dr. sc. Ivica Smojver

Statement | Izjava

I hereby declare that I have made this thesis independently using the knowledge acquired during my studies and the cited references.

Izjavljujem da sam ovaj rad radio samostalno koristeći znanja stečena tijekom studija i navedenu literaturu.

Zagreb, 2018   Ivan Pađen

Contents

List of Figures

List of Tables

List of Symbols

Greek Symbols

δ_M	m	Molecular film thickness
δ_T	m	Thermal film thickness
ϵ	m^2/s^3	Turbulent kinetic energy dissipation rate
Γ	m^2/s	Diffusivity
Λ	m	Wave length
λ	W/(mK)	Thermal conductivity coefficient
μ	N/(m^{2}s)	Molecular viscosity coefficient
ν	m^2/s	Kinematic viscosity
ν_{ki}	-	Stoichiometric coefficient of species k in reaction i
Ω	1/s	Wave growth rate
ρ	kg/m^3	Density
σ_{ji}	N/m^2	Stress tensor
τ_a	s	Breakup time
τ_{ji}	N/m^2	Viscous stress tensor
φ	variable	Arbitrary scalar variable
ζ	-	Velocity scale ratio

Latin Symbols

$\dot{r}$	kmol/m³s	Reaction rate
A	variable	Arrhenius law pre-exponential factor
B_M	-	Spalding mass number
B_T	-	Spalding heat number
c	-	Progress variable
c	mol/m³	Molar concentration
D_{ji}	N/m²	Deformation tensor
e	J/kg	Specific total energy
E_a	J/kg	Activation energy
F	N	Force
k	m²/s²	Turbulent kinetic energy
k_{b}	variable	Backward reaction rate constant
k_{f}	variable	Forward reaction rate constant
K_{c_i}	variable	Equilibrium constant in concentration units for reaction i
L	m	Turbulent time scale
M	kg/kmol	Molar mass
P_k	J/kg	Turbulent kinetic energy production
q_v	J/kg	Specific energy
q_v	J/m³	Energy density
r	m	Radius
S_{Y_k}	kg/s	Mass source of species k

T	K	Temperature
T	s	Turbulent time scale
u	m/s	Velocity
W_k	kg/kmol	Molecular weight of species k
Y_i	kg/kg	Mass fraction
Z	-	Mixture fraction

Abbreviations

CFD	Computational Fluid Dynamics
DDM	Discrete Droplet Method
EL	Euler Lagrangian
FGM	Flamelet-Generated Manifold
GGPR	General Gas Phase Reactions
HEFA	Hydroprocessed Esters and Fatty Acids
SOI	Start of Injection

Sažetak

U ovome radu izvršena je analiza podobnosti metode pojednostavljenja kemijske kinetike za primjenu u mlaznim motorima. Reakcijski mehanizam aviogoriva JP-10 korišten je za simulacije izgaranja u bačvastoj komori za izgaranje. Proces izgaranja prvotno je modeliran koristeći pristup kemijske kinetike, u kojem je dodatni set transportnih jednadžbi riješen za svaku kemijsku vrstu. Zatim je korišten pristup tabličnih podataka propagacije plamena, preciznije AVL TABKIN™ model izgaranja temeljen na pristupu engleskog naziva *Flamelet-Generated Manifold*. Izgaranje je započeto modelom iskre koji uvodi energiju u određene točke u prostoru iznosa većeg od energije aktiviranja reakcije goriva. Ubrizgavanje je opisano Euler-Lagrangeovom metodom diskretnih čestica, te je korišten WAVE model raspršivanja kapljevine. Prikazani su dobiveni rezultati s naglaskom na kompromis između odstupanja rezultata i uštede u vremenu računanja. Računalne simulacije izvršene su u softverskom paketu AVL FIRE™ , dok su tablice propagacije plamena izrađene u alatu AVL TABKIN™ *Table Generation Tool*.

Ključne riječi: RDF, mlazni motor, izgaranje, kemijska kinetika, tablični pristup, tabkin

Abstract

In this thesis a feasibility analysis of a chemistry simplification approach for jet engine applications was performed. A reaction mechanism of the JP-10 aviation fuel was used to conduct combustion simulations in a can-type combustion chamber. The combustion process was initially modeled using the general gas phase reactions approach, where an additional set of transport equations was solved for each chemical species involved. Afterwards, the tabulated chemistry approach was employed, specifically the Flamelet-Generated Manifold based AVL TABKIN™ combustion model. The ignition was initiated with the spark ignition model that introduces energy in certain points which is beyond the fuel activation energy. The fuel injection was described by the Euler-Lagrangian discrete particle approach, where the WAVE model was employed for liquid atomization. Obtained results were presented, with the emphasis on the compromise between result deviation and reduction in turnaround times. Simulations were performed with the computational dynamics software AVL FIRE™ and the chemistry tabulation was performed by AVL TABKIN™ Table Generation Tool.

Keywords: CFD, jet engine, combustion, chemical kinetics, chemistry tabulation, tabkin

Prošireni sažetak

Računalna dinamika fluida (RDF) predstavlja moderni inženjerski alat koji ubrzava proces razvoja projekta te, jednako bitno, smanjuje ukupne troškove. Numeričko modeliranje procesa izgaranja je zahtjevan izazov koji kombinira polja dinamike fluida, prije svega višefaznog strujanja, i kemije. Pristup kemijske kinetike daje detaljan uvid u kemijske procese tijekom izgaranja. No takav je pristup računalno zahtjevan što dovodi do razvoja metoda ubrzavanja proračuna. Primjer takve metode je pristup tabeliranih podataka propagacije plamena (eng. *Flamelet Generated Manifold* - FGM) koja omogućuje ubrzavanje proračuna detaljnih reakcijskih mehanizama. Cilj ovog rada je ispitati primjenjivost FGM-a na simuliranje procesa u komori izgaranja mlaznog motora.

Matematički model

Strujanje fluida moguće je opisati kombiniranjem zakona o očuvanju mase (jednadžba kontinuiteta), zakona o očuvanju količine gibanja (Navier-Stokesove jednadžbe) i zakona o očuvanju energije (prvi zakon termodinamike). Zakoni o očuvanju mogu se sažeti u oblik opće transportne jednadžbe proizvoljnog fizikalnog svojstva:

$$\frac{\partial}{\partial t}\left(\rho\varphi\right) + \frac{\partial}{\partial x_j}\left(\rho\varphi u_j\right) = \frac{\partial}{\partial x_j}\left(\Gamma_\varphi \frac{\partial \varphi}{\partial x_j}\right) + S_\varphi, \qquad (0.1)$$

gdje je prvi član tranzijentni član, drugi član konvekcijski, treći difuzijski te četvrti član izvor ili ponor fizikalnog svojstva φ. Osim za strujanje fluida, opća transportna jednadžba vrijedi i za očuvanje mase kemijskih vrsta, gdje izvorski član predstavlja kemijske reakcije - stvaranje i uništavanje kemijskih vrsta.

Modeliranje turbulencije

Strujanje može biti laminarno, prijelazno ili turbuluentno, no gotovo sva strujanja u inženjerskoj prirodi su turbulentna. Turbulencija je modelirana koristeći Reynoldsovo osrednjavanje Navier-Stokesovih jednadžbi, gdje je Reynoldsov tenzor naprezanja, temeljen na Bussineqovoj hipotezi, riješen koristeći k-ζ-f model turbulencije.

Višefazno strujanje

Višefazna strujanja podrazumijevaju strujanja koja sadrže dvije ili više komponenti na skali iznad molekularne razine. Kod mlaznog motora, u sferu višefaznog strujanja spadaju proces ubrizgavanja tekućeg goriva (proces spreja), miješanja goriva sa zrakom te isparavanja. U ovom radu korišten je Euler Lagrangeov pristup diskretnih kapljica koji opisuje kapljevitu fazu diskretnim kapljicama. Kapljice, slične po veličini i fizikalnim svojstvima, grupirane su u parcele čije se trajektorije i brzine prate kroz domenu koristeći Lagrangeovu formulaciju. S druge strane, plinovita faza tretirana je kao kontinuum i opisana transportnim jednadžbama u Eulerovoj formulaciji. Trajektorija i brzina pojedine parcele izvedena je iz drugog Newtonovog zakona:

$$m_p \frac{du_{id}}{dt} = \sum F_i, \tag{0.2}$$

gdje m_p označava masu parcele, a $\sum F_i$ sumu svih sila koje djeluju na tu parcelu.

Podmodeli spreja

Kako bi se što točnije opisao proces spreja, koriste se određeni podmodeli poput primarnog i sekundardnog raspadanja, isparavanja, deformacije kapljica, sudaranja, spajanja te turbulentne disperzije.

U ovome radu korišten je WAVE model raspadanja kapljica koji pretpostavlja raspad tekućeg mlaza usred djelovanja aerodinamičkih sila. Brzina raspadanja kapljice, odnosno brzina smanjenja radijusa, dana je izrazom:

$$\frac{dr}{dt} = -\frac{r - r_{\text{stable}}}{\tau_a}, \tag{0.3}$$

gdje r_{stable} predstavlja radijus kapljice nakon raspada, a τ_a vrijeme potrebno za raspad. Radijus novonastale kapljice proporcionalan je valnoj duljini najbrže rastućeg vala Kelvin-Helmholtzovih nestabilnosti na površini kapljice:

$$r_{\text{stable}} = \Lambda \cdot C_1, \tag{0.4}$$

dok vrijeme raspada uvodi u jednadžbu brzinu širenja vala Ω:

$$\tau_a = \frac{3.726\, C_2\, r}{\Lambda \Omega}. \tag{0.5}$$

U jednadžbama iznad, C_1 i C_2 označavaju konstante modela.

Osim raspadanja, korišten je i Abramzon-Sirignano model isparavanja, temeljen na klasičnoj teoriji filma. Utemeljen je na pretpostavci jednolike raspodjele temperature po površini kapljice sferičnog oblika.

Na kraju, korišten je model turbulentne disperzije koji uzima u obzir međudjelovanje turbulentnih vrtloga i kapljica, što u konačnici utječe na promjenu trajektorije kapljice.

Modeliranje izgaranja

Proces izgaranja modeliran je koristeći kemijski mehanizam i dva pristupa modeliranju kemijskih reakcija:

1. pristup kemijske kinetike,

2. pristup tabeliranih podataka propagacije plamena AVL TABKIN™ , temeljen na FGM-u.

Kemijskom kinetikom, odnosno generalnim reakcijama plinovite faze (eng. *General Gas Phase Reactions* - GGPR), rješavaju se transportne jednadžbe za sve kemijske vrste kemijskog mehanizma, pri čemu se izvorski član (nastajanje i uništavanje kemijskih vrsta) modelira pomoću empirijske Arrheniusove jednadžbe [15]:

$$k_{\text{f}} = A\, T^b \cdot \exp\left(-\frac{E_a}{RT}\right), \tag{0.6}$$

u kojoj je k_f brzina kemijske reakcije, A i b konstante modela te E_a energija aktivacije. A, b i E_a su eksperimentalno dobiveni podaci.

Pristup tabeliranih podataka propagacije plamena AVL TABKIN™ modelira višedimenzijski plamen kao skup jednodimenzijskih plamena. Određeni podaci svojstveni za jednodimenzijske plamene spremljeni su u tabličnom obliku te su interpolirani prilikom simulacija izgaranja. Podaci u tabličnom obliku su:

- tlak,

- temperatura svježeg zraka,

- omjer smjese,

- varijabla napretka,

- količina zaostalih plinova (eng. *Exhaust Gas Recirculation* - EGR) i

- parametar kompozicije goriva.

Omjer smjese skalarna je veličina koja određuje smjesu zraka i goriva. Iznos omjera smjese je nula u oksidansu i jedan u gorivu. Varijabla napretka predstavlja skalar koji opisuje napredak izgaranja i plamena, tj. promjenu reakcije iz stanja svježe, neizgorene smjese u izgoreni plin. Ovaj pristup omogućuje smanjenje broja kemijskih vrsta na 5, od kojih je jedna gorivo koje, preko tabeliranih podatka, sadrži sve podatke detaljnog kemijskog mehanizma na kojem je bazirano.

Modeliranje goriva

U ovome radu korišteno je sintetičko gorivo za vojne primjene, naziva JP-10. Gorivo je modelirano detaljnim kemijskim mehanizmom [16] koji se sastoji od 36 kemijskih vrsta uključenih u 174 elementarne reakcije. Ovaj model izveden je iz eksperimentalnih podataka, ali i teoretskih pretpostavka, što je uneslo ograničenja u model. Model je primjenjiv za temperature od 1000 K do 2500 K, tlakove između 1 i 100 bar te ekvivalentne omjere zraka manje od 2.

Numeričke postavke

Komercijalni programski paket AVL FIRE™ korišten je za numeričke simulacije teoretske komore za izgaranje mlaznog motora. Dimenzije i 3D model komore prikazani su na slikama 0.1 odnosno 0.2.
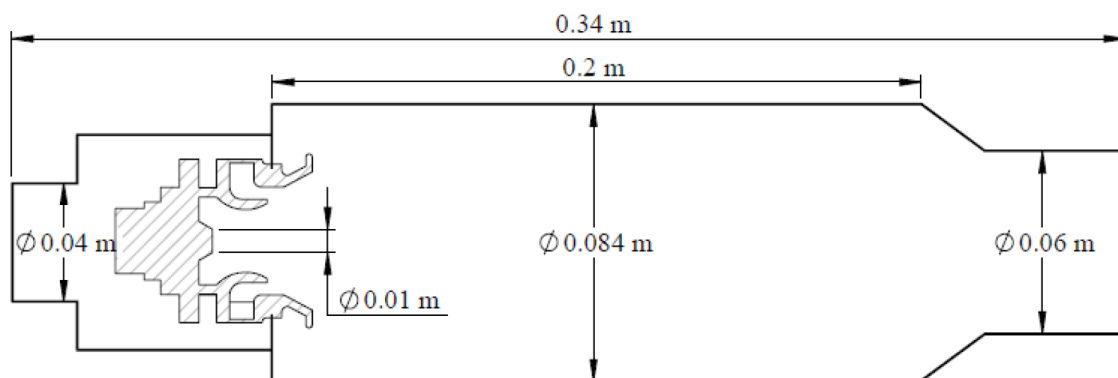
Slika 0.1: Dimenzije komore za izgaranje [43]
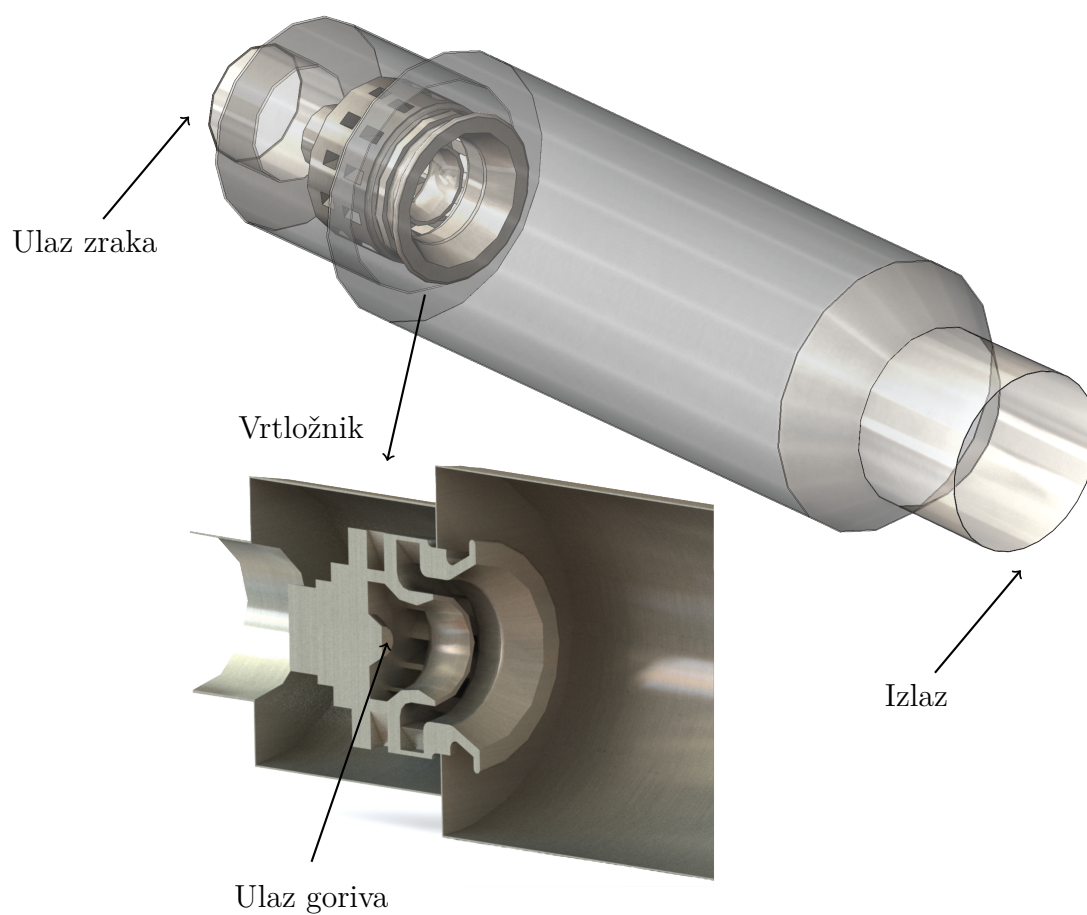
Slika 0.2: CAD model komore

U nastavku su dani relevantni podaci modeliranih računalnih domena, početni i rubni uvjeti, kao i postavke vezane za izgaranje.

Računalne domene

Tri računalne domene izrađene su za test utjecaja mreže. Mrežama su dani nazivi "gruba", "srednja" i "gusta", ovisno o broju kontrolnih volumena. Tablica 0.1 sadrži osnovne podatke o korištenim računalnim domenama.

Tablica 0.1: Podaci računalnih domena korištenih za ispitivanje utjecaja kvalitete mreže

Gustoća mreže	Najmanja dimenzija KV[m]	Najveća dimenzija KV[m]	Ukupan broj KV
Gruba	0.0008025	0.00321	336042
Srednja	0.0006581	0.00263	460415
Gusta	0.0005062	0.002025	701823

Početni i rubni uvjeti

Iznosi rubnih i početnih uvjeta mogu se iščitati iz tablica 0.2 i 0.3.

Tablica 0.2: Rubni uvjeti

Maseni protok zraka	0.8 kg/s
Temperatura zraka	650 K
Maseni protok goriva	0.023 kg/s
Temperatura goriva	300 K
Zid	Adijabatski RU (0 W/m²)
Izlazni tlak	9.12 bar

Tablica 0.3: Početni uvjeti

Tlak	9.12 bar
Temperatura	650 K
Turbulentna skala	0.001 m
Turbulentna kinetička energija	0.001 $\mathrm{m^2 s^{-2}}$

Površine na kojima su definirani rubni uvjeti dane su na slici 0.3.
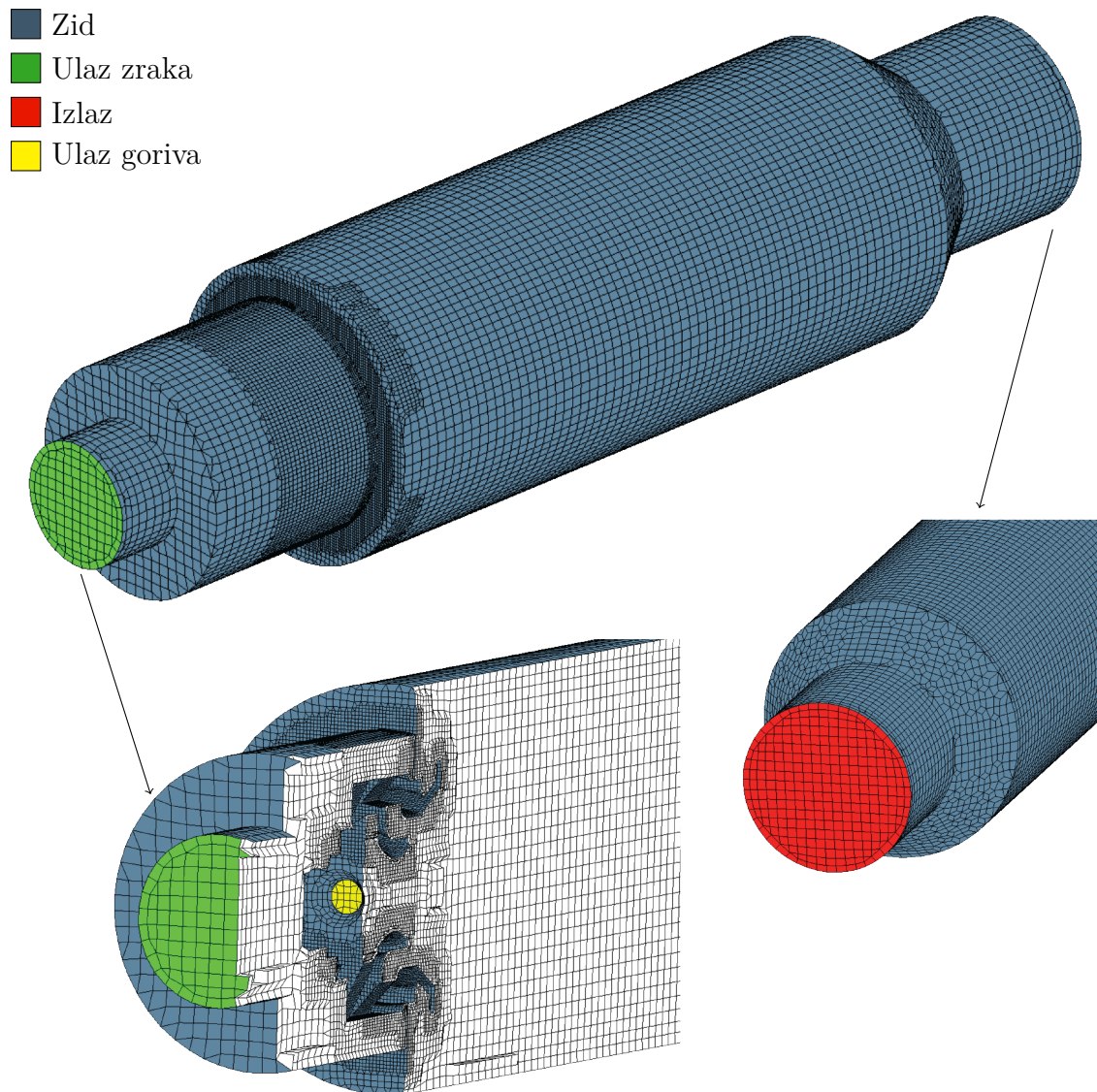
Slika 0.3: Selekcije rubnih uvjeta

Postavke spreja

Točka središta izlazne mlaznice spreja udaljena je 0.062 m po aksijalnoj osi od početka komore (ulaza zraka). Kut spreja postavljen je na 20°. Početak ubrizgavanja goriva je 2 ms nakon početka simulacije. Vanjski promjer izlazne mlaznice iznosi 1 mm, dok unutarnji promjer 0.8 mm. Maksimalna veličina parcele na izlazu iz mlaznice je 150 μm i ukupno 27 parcela ubrizgava se u domenu u svakom vremenskom koraku.

Zapaljenje goriva

Zapaljenje smjese goriva i zraka osigurava se uvođenjem energije u domenu putem 8 jednoliko raspoređenih iskri. Iskre, koje simuliraju svjećice, postavljene su na 100 mm od ulaza goriva. Tablica 0.4 daje podatke o iskri, gdje energetski faktor označava parametar modela koji definira intenzitet iskrenja - veće vrijednosti dovode do većeg lokalnog porasta temperature.

Tablica 0.4: Postavke iskre

Početak iskre	0.0031 s
Veličina jezgre plamena	0.008 m
Trajanje zapaljenja	0.0015 s
Energetski faktor	10 (GGPR); 20 (TABKIN)

Rezultati

Prvo je proveden test utjecaja mreže, gdje su promatrana polja temperature i tlaka. Zatim je provedena usporedna analiza GGPR-a i TABKIN-a, točnije analiza temperaturnih polja uzdužnih i poprečnih presjeka za različite vremenske trenutke te srednja temperatura i tlak tijekom simulacija.

Test utjecaja mreže

U nastavku su prikazani rezultati testa utjecaja mreže za polja brzine, što je prikazano na slici 0.4, i temperature (slika 0.5) u trenutku t=0.2 ms (početak ubrizgavanja goriva). Iz slika se može zaključiti kako sve tri mreže daju približno jednake rezultate, stoga je gruba mreža korištena za sve daljnje proračune.

Brzina [m/s]

0   450

Gusta

Srednja

Gruba
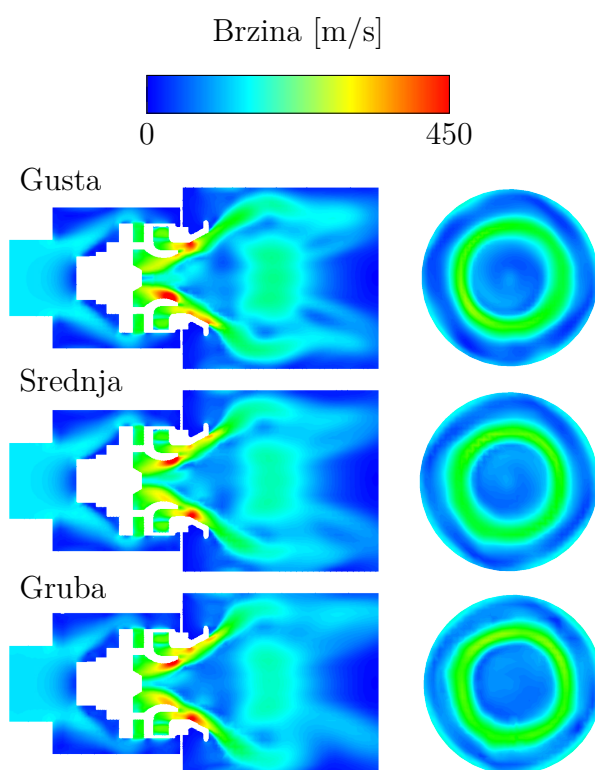
Slika 0.4: Test utjecaja mreže na polje brzine

Temperatura [K]

300   750

Gusta

Srednja

Gruba
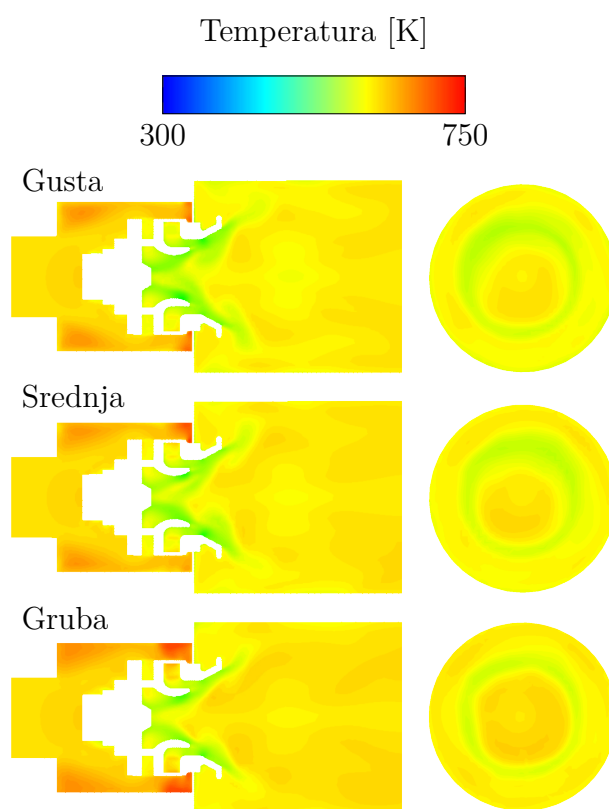
Slika 0.5: Test utjecaja mreže na polje temperature

Formiranje spreja

Ubrizgavanje goriva započinje 2 ms nakon početka simulacije. Stvaranje konusa spreja i početak isparavanja goriva vidljivi su na slici 0.6. Kapljice spreja obojane su prema promjeru, dok je ispareno gorivo prikazano prozirnom plavom površinom.
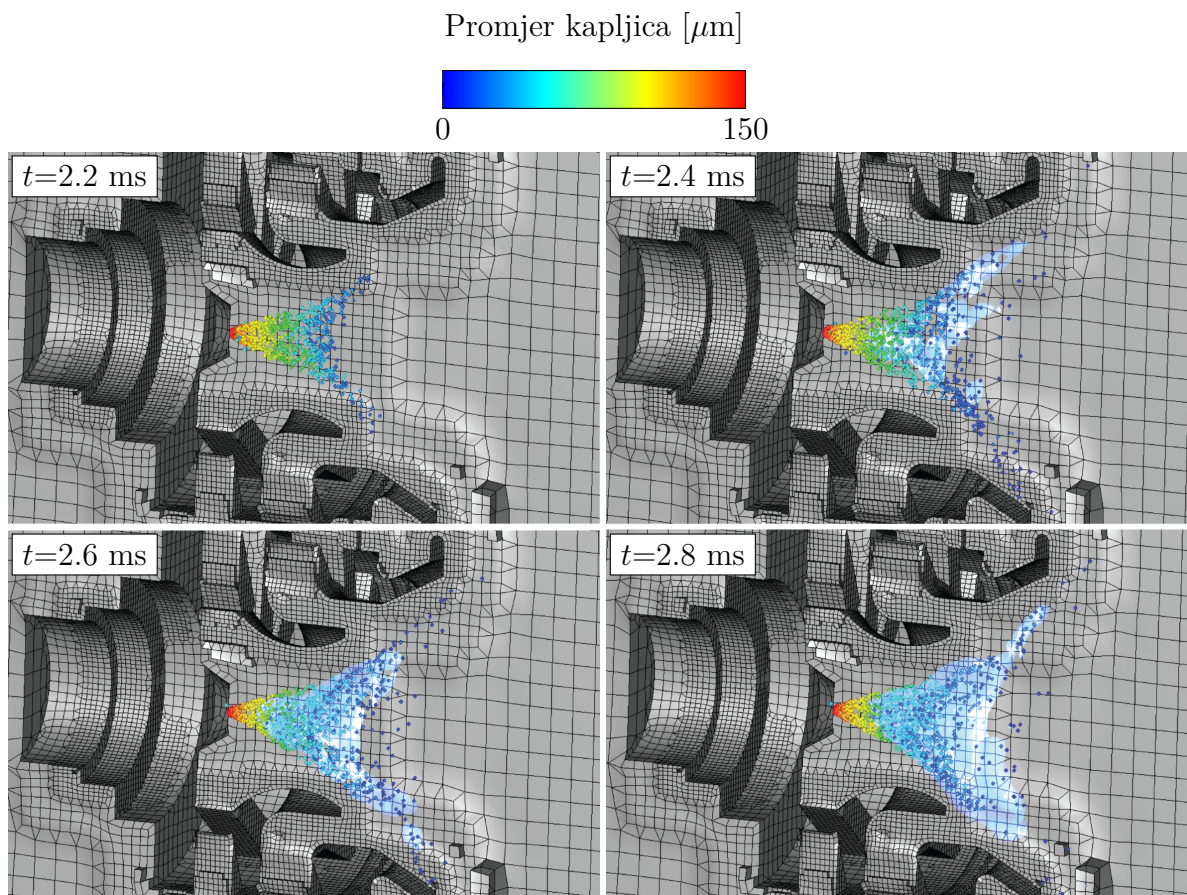
Slika 0.6: Ubrizgavanje i isparavanje goriva

Izgaranje

Zapaljenje smjese, tj. početak iskre, je na 3.1 ms od početka simulacije, odnosno 1.1 ms od početka ubrizgavanja goriva. Lijeva strana slike 0.7 prikazuje promjenu temperaturnog polja za GGPR, dok desna za TABKIN. Promjena srednje temperature i tlaka u komori dana je slikom 0.8. Iz slike i grafa uočava se kako GGPR intenzivnije dolazi u kvazistacionarno stanje (veći nagib krivulje temperature), što je posljedica različitog modeliranja iskre. U GGPR-u, energetski faktor iskre postavlja se u jednadžbu očuvanja energije, dok u TABKIN-u u varijablu napredovanja. Nadalje, temperaturna polja određenih poprečnih presjeka u kvazistacionarnom stanju vidljiva su na slici 0.9.

Temperatura [K]

650   2,200

GGPR   TABKIN

3.2 ms

3.6 ms

4.2 ms

4.8 ms

6.8 ms

12 ms
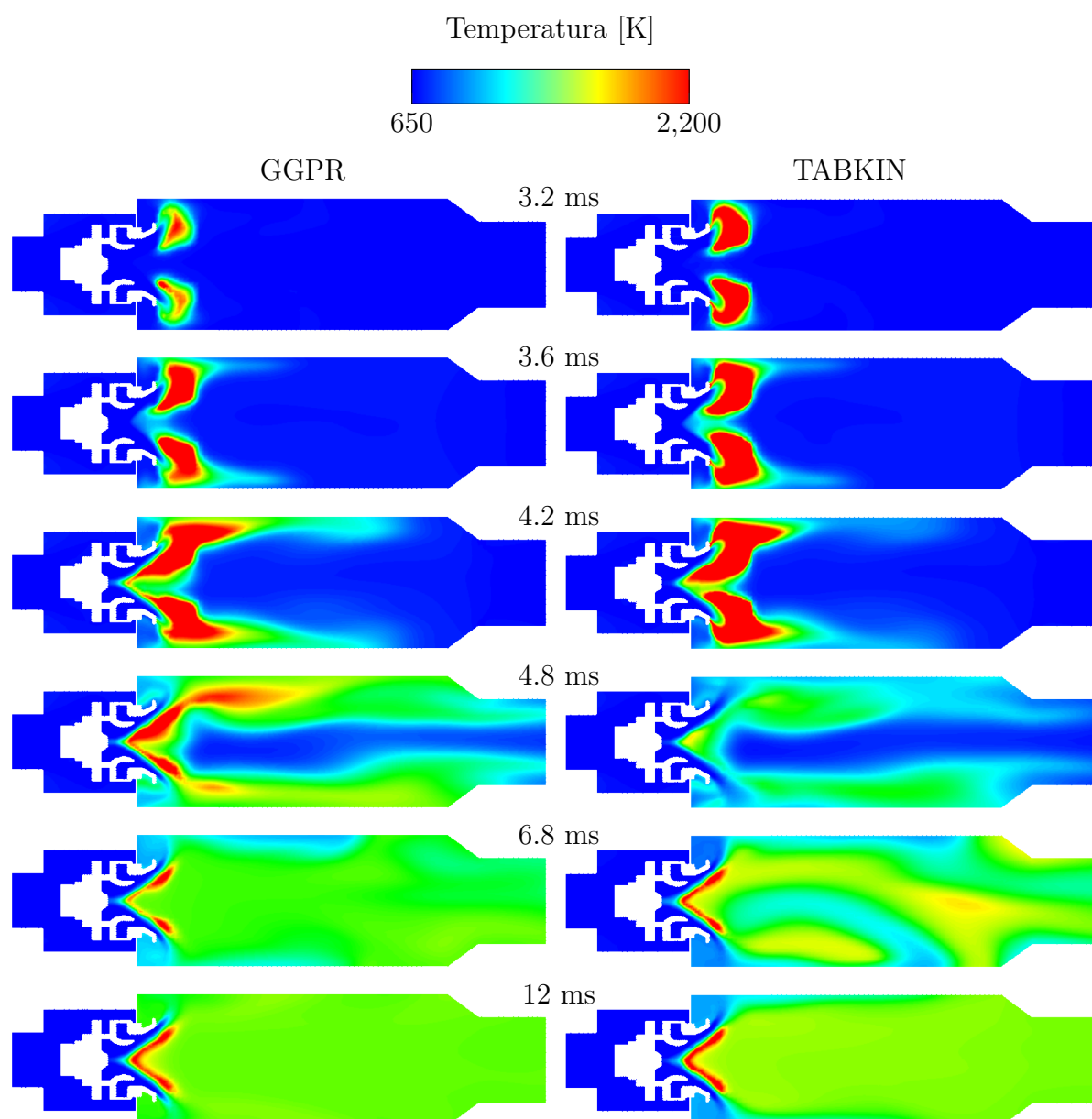
Slika 0.7: Usporedba temperaturnih polja tijekom izgaranja
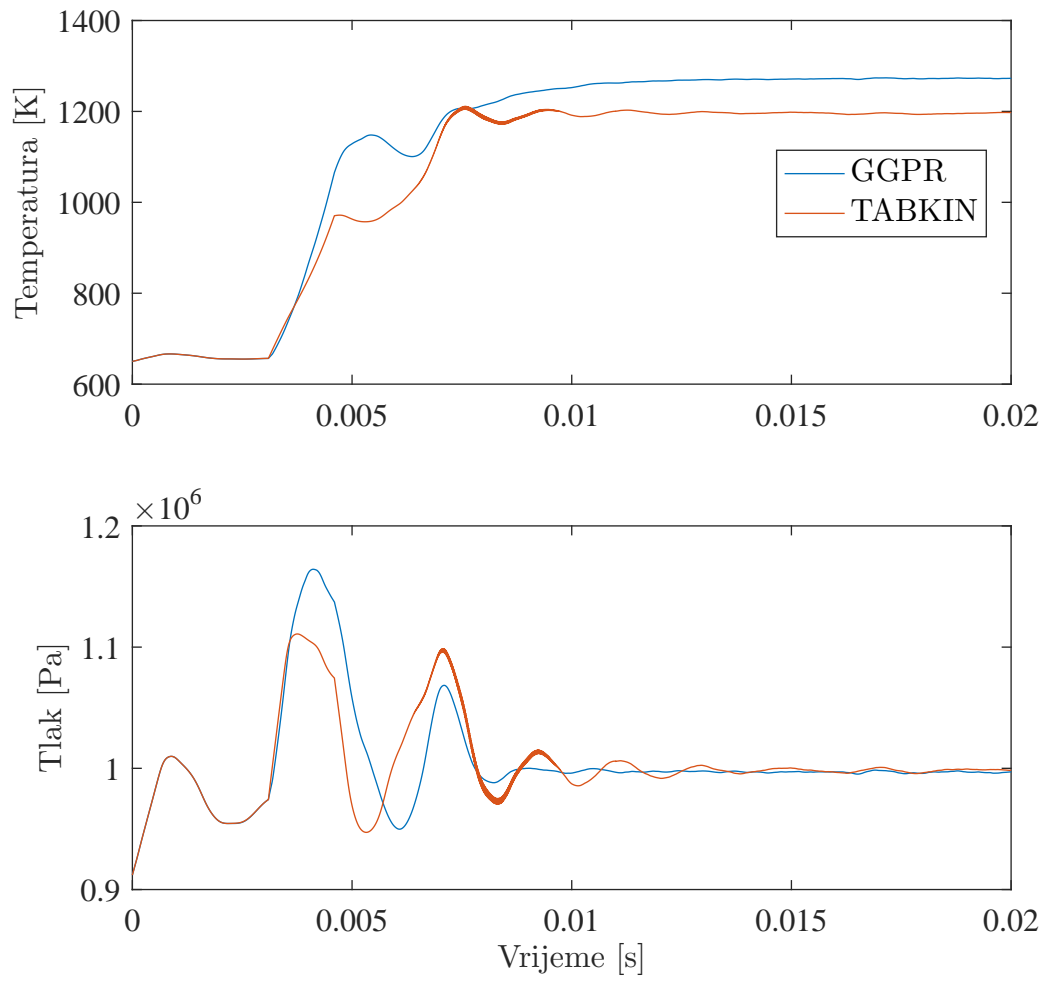
Slika 0.8: Promjena srednje temperature i tlaka
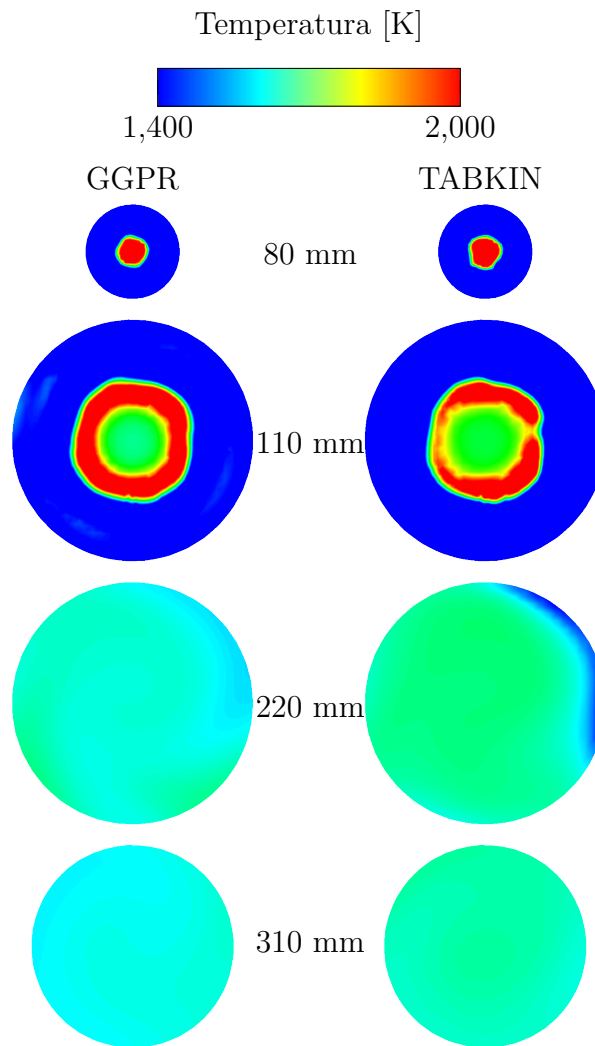
Slika 0.9: Temperaturna polja poprečnih presjeka u kvazistacionarnom stanju

Poprečni presjeci temperaturnih polja u primarnoj zoni izgaranja pokazuju dobra po-dudaranja, no razlike u rezultatima veće su u sekundarnoj zoni. Ta razlika je vidljiva i kod srednjih temperatura te iznosi 5.5%, dok je razlika srednjih tlakova zanemariva. S druge strane, TABKIN simulacija traje 5.55 puta kraće od GGPR simulacije, što je značajna ušteda u vremenu.

1 | Introduction

Jet engines have seen major developments in the past decades, leading to modern fuel efficient/low emission high-bypass turbofans. However, more stringent emission regulations and increasing fuel prices are calling for further development, raising the bar when it comes to efficiency and pollutant emissions. Computational Fluid Dynamics (CFD) represent a modern engineering tool which is able to accelerate the development process and, equally important, lower overall costs. Numerical modeling of a combustion process is a demanding challenge, combining the fields of fluid dynamics, particularly multiphase flows, and chemistry. Chemical kinetics with detailed reaction mechanisms is capable of providing a comprehensive insight into the chemical aspect of the process. Nevertheless, it is computationally intense, yielding a number of proposed reduction techniques, one of them being the Flamelet Generated Manifold (FGM) which has become a potential candidate for the industry applications. The aim of this thesis is to investigate the applicability of FGM in jet engine combustor simulations.

1.1. Jet Engine

The jet engine operates on account of the Third Newton's law of motion stating that for every action there is an equal and opposite reaction. Action, in this case, is an accelerated stream of air or gas expelled out of the engine at high velocity. Reaction is the propelling force - thrust. The energy required to instigate the jet acceleration is introduced through combustion and, in case of turbine powered engine, increase of the pressure energy. The heat and the pressure are subsequently turned into kinetic energy which ultimately results in thrust. The most general classification divides jet engines into two types: airbreathing and non-airbreathing, depending on the source

of the oxidant. While non-airbreathing are essentially rocket engines, airbreathing jet engines can be further divided into:

- turbine powered (turbojets, turbofans, turboprops, turboshafts);

- ram powered (ramjets, scramjets);

- pulsejets.

The turbine powered engines use a turbine-driven compressor to raise the pressure energy required for combustion. The vast majority of jet propelled aircraft use this type of engine. Ram powered engines only use the ram pressure for combustion. To attain return pressures high enough for efficient combustion, a ramjet-powered aircraft has to travel at high speeds, with the best operating range between Mach 2 and Mach 4.

A typical turbine powered jet engine is based on the Brayton cycle. The idealized gas turbine engine for subsonic speeds is shown in Figure 1.1.
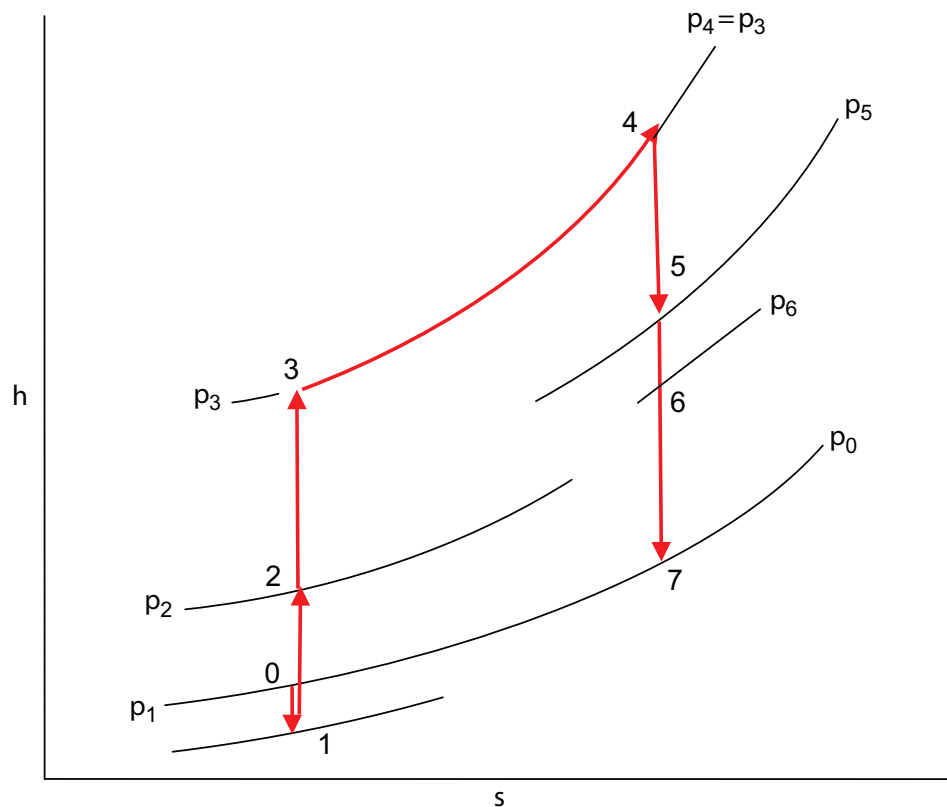
Figure 1.1: Idealized turbojet cycle diagram for subsonic flight [1]

The cycle consists of the following segments :

- isentropic compression,

  - in inlet, 1-2;

  - in compressor 2-3;

- isobaric combustion, in combustor 3-4;

- isentropic expansion,

  - in turbine, 4-5;

  - in nozzle 5-7;

In subsonic flights, the free stream pressure p_0 is lower than the inlet pressure p_1 as the streamtube area contracts at the entrance of the inlet. On the other hand, in supersonic flight, p_1 is always greater than p_0 because of a shock wave in and around the inlet lip [1].

Major components of the turbojet engine and their relation to the cycle diagram are given in Figure 1.2.
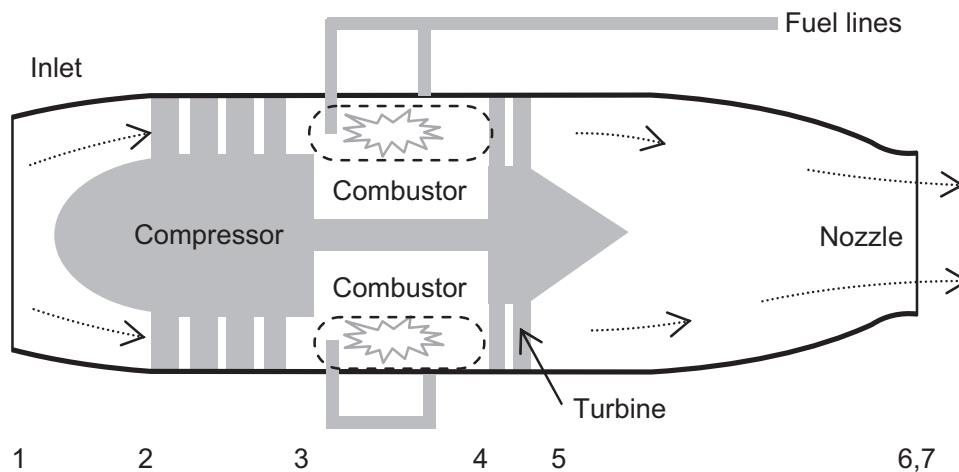
Figure 1.2: Schematic diagram of a typical turbojet engine [1]

The following sections will give more details on the major components in relation to cycle segments.

1.1.1.   Compression

The compression process of turbine powered jet engines is divided between the inlet and the turbine-driven compressor. In addition, turbofans have a fan in front of the

compressor, accelerating most of the air from inlet rearwards through a bypass. For subsonic speeds, the inlet provides only a fraction of the total pressure rise during the compression. However, as the flight speed increases, the contribution of the ram air from the inlet becomes more substantial. This in turn lowers the required work for the compressor, increasing the thrust and engine efficiency.

Inlet

The inlet is the first component on the engine, directly in the way of the free stream. Its main goal is to prepare the flow for the compressor, or, in case of ramjets and pulsejets, directly for the combustor. The major attributes of the inlet may be listed as follows [1]:

- handle a wide range of mass flow,

- duct air to the engine with low total pressure loss and low drag,

- diffuse the flow over its length to high pressure and low Mach number,

- minimize distortions in the flow field exiting the inlet, and

- be of low weight, small size and mechanically simple.

To ensure the maximum pressure recovery, the inlet has to be appropriately designed. For subsonic speeds it is commonly in a form of the pitot inlet. The design of the inlet becomes more complex for when higher speeds are in question, with cones, ramps or bumps for shock waves, and boundary layer diverters.

Compressor

Two basic types of compressors are used in jet engines. The centrifugal compressor, shown in Figure 1.3, above, operates on directing the flow in the radial direction by the impeller, thus raising its velocity and pressure. The pressure is then further increased through a diffuser. The main advantage of the centrifugal compressor is a high pressure rise in a single stage. It is also easier to develop, manufacture and maintain than the axial compressor, all of which made it appealing to use in light jets. On the contrary, radially exiting flow requires excessive turning, leading to flow distortion and pressure

drops. For this reason multistage centrifugal compressors are rarity. To overcome this disadvantage, some small jet engines combine a stage of the centrifugal compressor with axial stages or a fan. Additionally, the larger cross section than the axial configuration makes them more prone to drag.

The second type is the axial compressor, shown in Figure 1.3, below, in which the air flows parallel to the axis of rotation through stages of rotor and stator blades. The pressure ratio is relatively low, at least two times lower than the centrifugal compressor, to avoid air breakaway and blade stall. Irrespective of the lower pressure ratio per stage, the total pressure rise of the axial compressor is much higher due to high number of stages. Higher pressure ratios allow higher thrust, which is the main reason why axial compressors have been used when a lot of propelling power is a necessity.
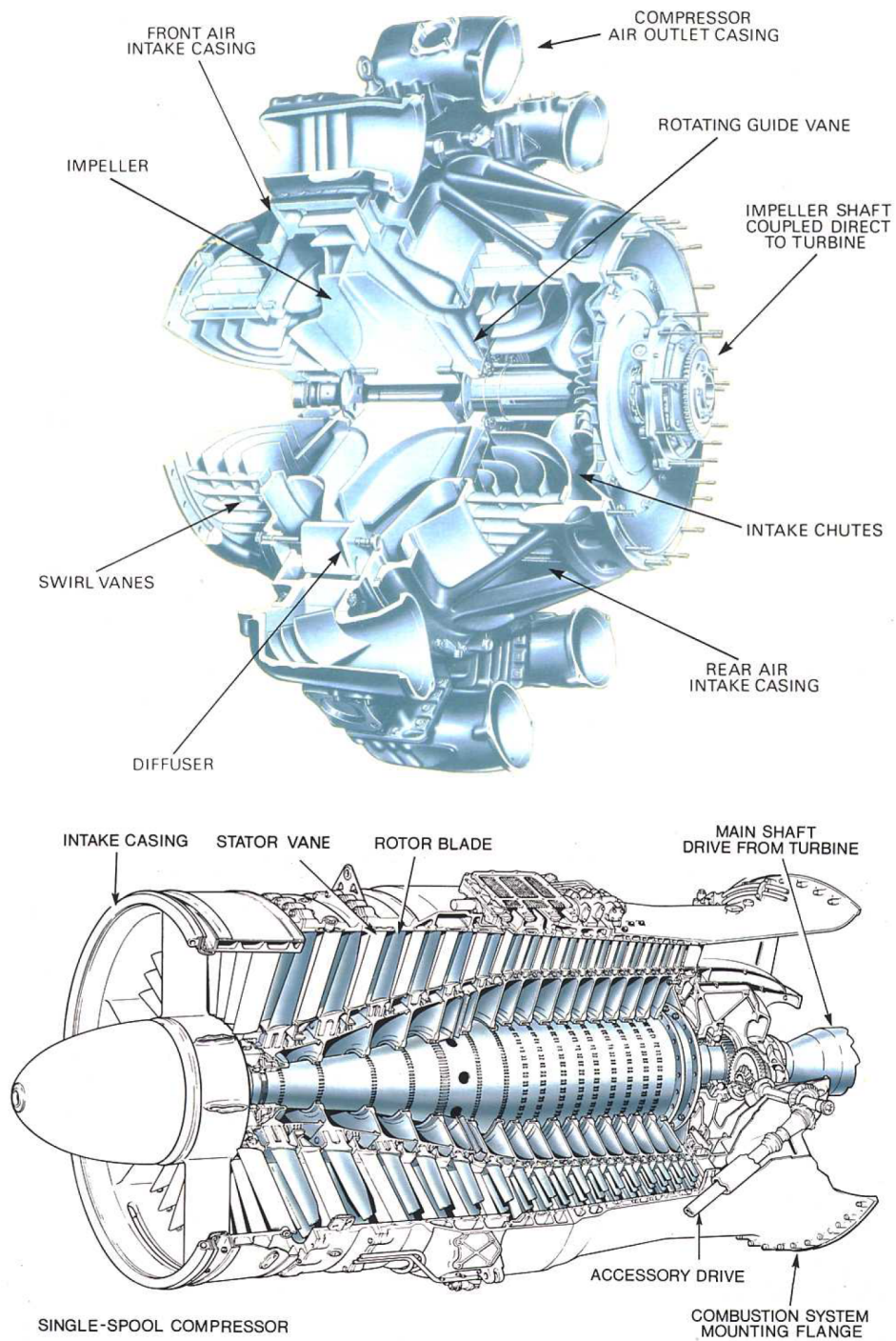
Figure 1.3: A typical centrifugal (above) and axial (below) compressor [2]

1.1.2. Combustion

The main goal of the combustion chamber is to provide stable and efficient combustion over a wide range of engine operating conditions, i.e.:

- provide full combustion with minimum pressure loss,

- operate without significant accumulation of deposits,

- ignite fuel readily,

- give reliable service over long periods of time [1].

The air from the compressor enters a diffuser and splits into primary (around 18% of total airflow) and secondary stream (around 82% of total airflow). The purpose of the diffuser is to slow down the stream as combustion of jet fuel takes place at low speeds. The primary air stream passes through swirl vanes to form a region of low velocity recirculation which stabilizes the flame and provides turbulence for better combustion. Fuel is injected at the exit of the swirler and together with the primary air ignites in the so-called primary zone. The secondary air enters the combustion chamber through perforated or slotted liner and cools the hot gases in order to protect the wall of the chamber as well as the turbine. This section of the chamber is called dilution or secondary zone. Figure 1.4 shows the air distribution through the combustor.
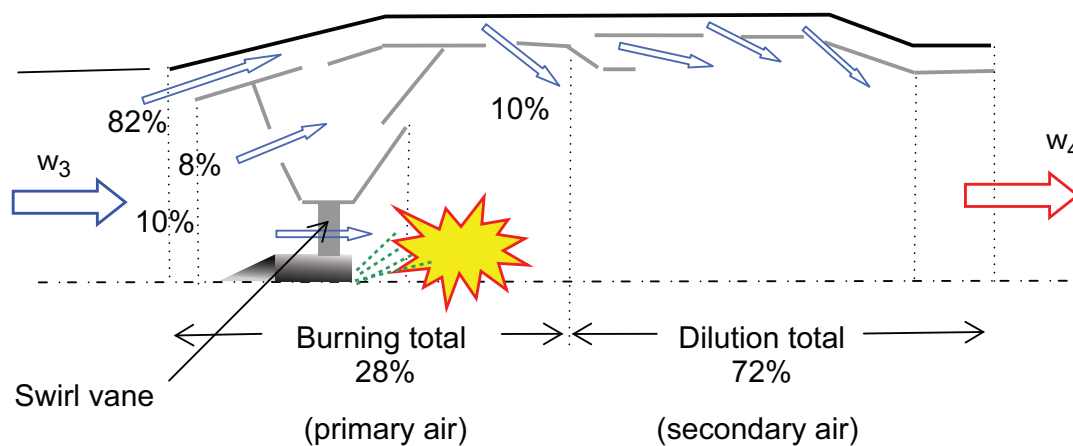
Figure 1.4: Apportionment of air in the typical combustor) [1]

Three types of combustors are typical for airbreathing jet engines. Figure 1.5 shows the can-type combustor, which is essentially a stack of self-contained cylindrical combustion chambers. The air from compressor is directed by ducts into individual chambers. These combustors are easy to maintain, as individual cans can be removed, omitting the need for turbine shaft removal. However, most modern jets don't use this type of combustors as they produce larger pressure drop and weigh more than their alternatives.
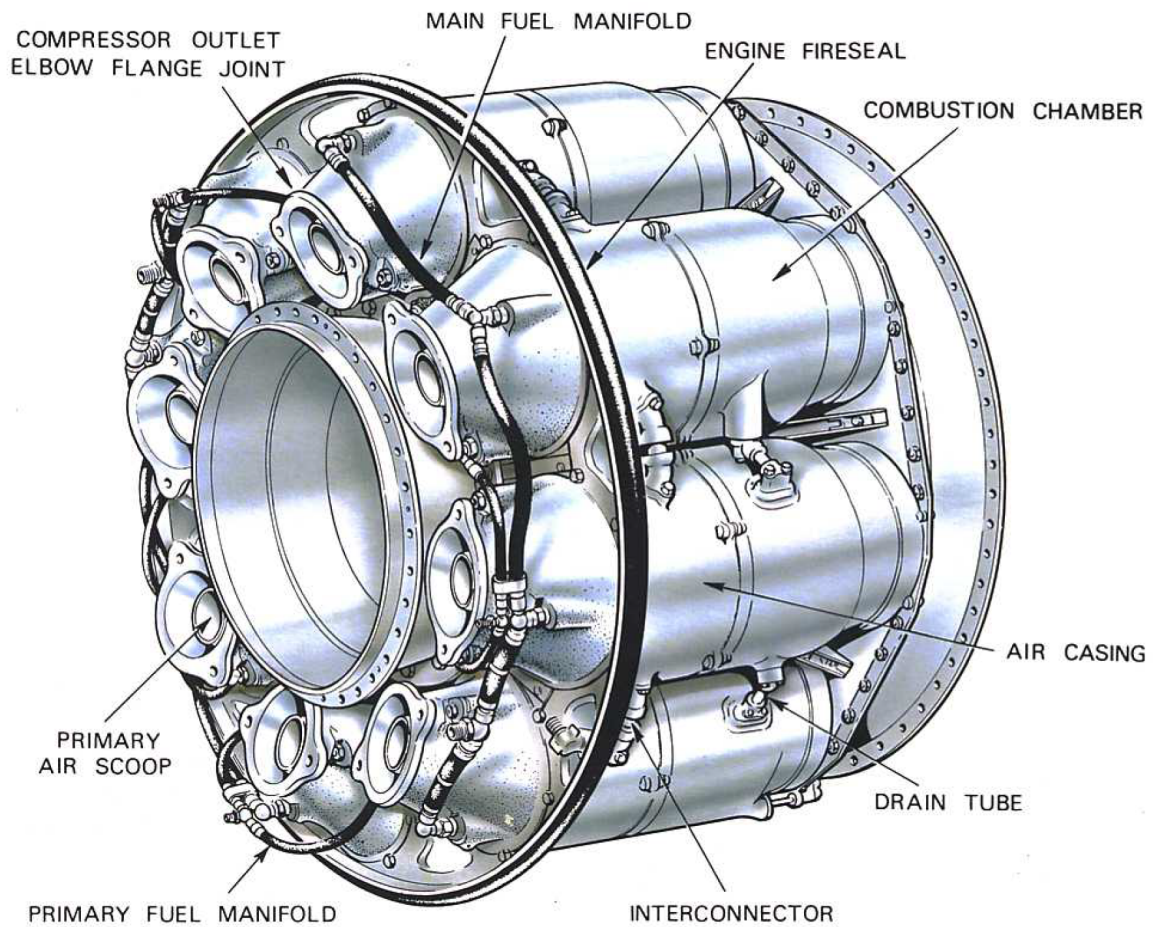
Figure 1.5: Can-type combustor [2]

The next type is the tubo-annular combustor, shown in Figure 1.6, where discrete flame tubes are connected together with interconnectors, allowing flame to travel between each tube. Such design allows more uniform temperature profile, lower pressure drops and lower weight than can combustors. Nonetheless, they are harder to maintain due to common casing.
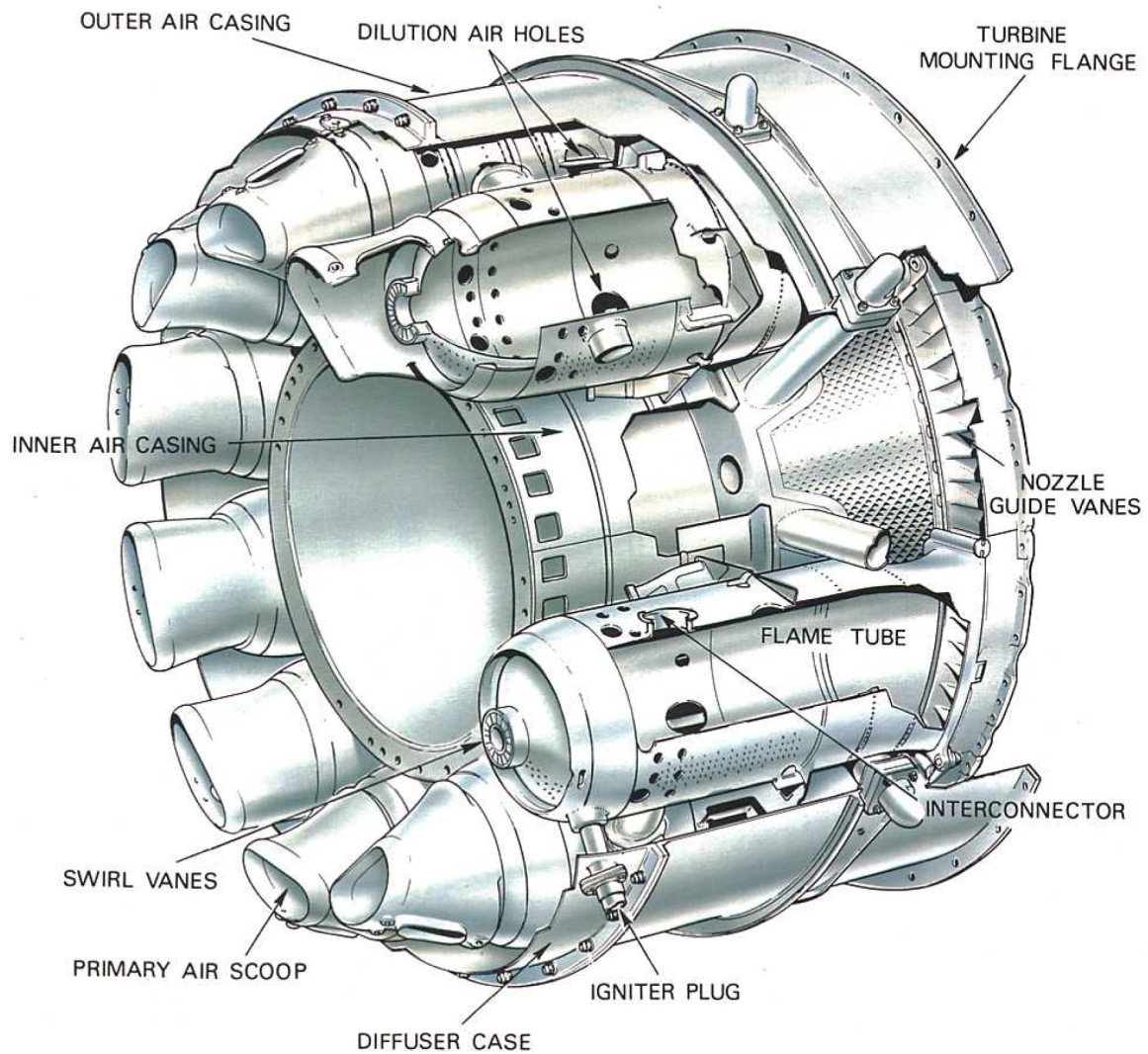
Figure 1.6: Tubo-annular combustor [2]

The last type is the annular combustor, shown in Figure 1.7. This type of combustor consists of a single flame tube, completely annular in form, contained in an inner and outer casing [2]. Annular combustors are light, have smaller wall area resulting in lesser amount of cooling air, have the most uniform temperature distribution and the smallest pressure drop in comparison to other combustor types. As can be seen, these combustors offer the most, making them the most widely used type of combustors in modern engines.
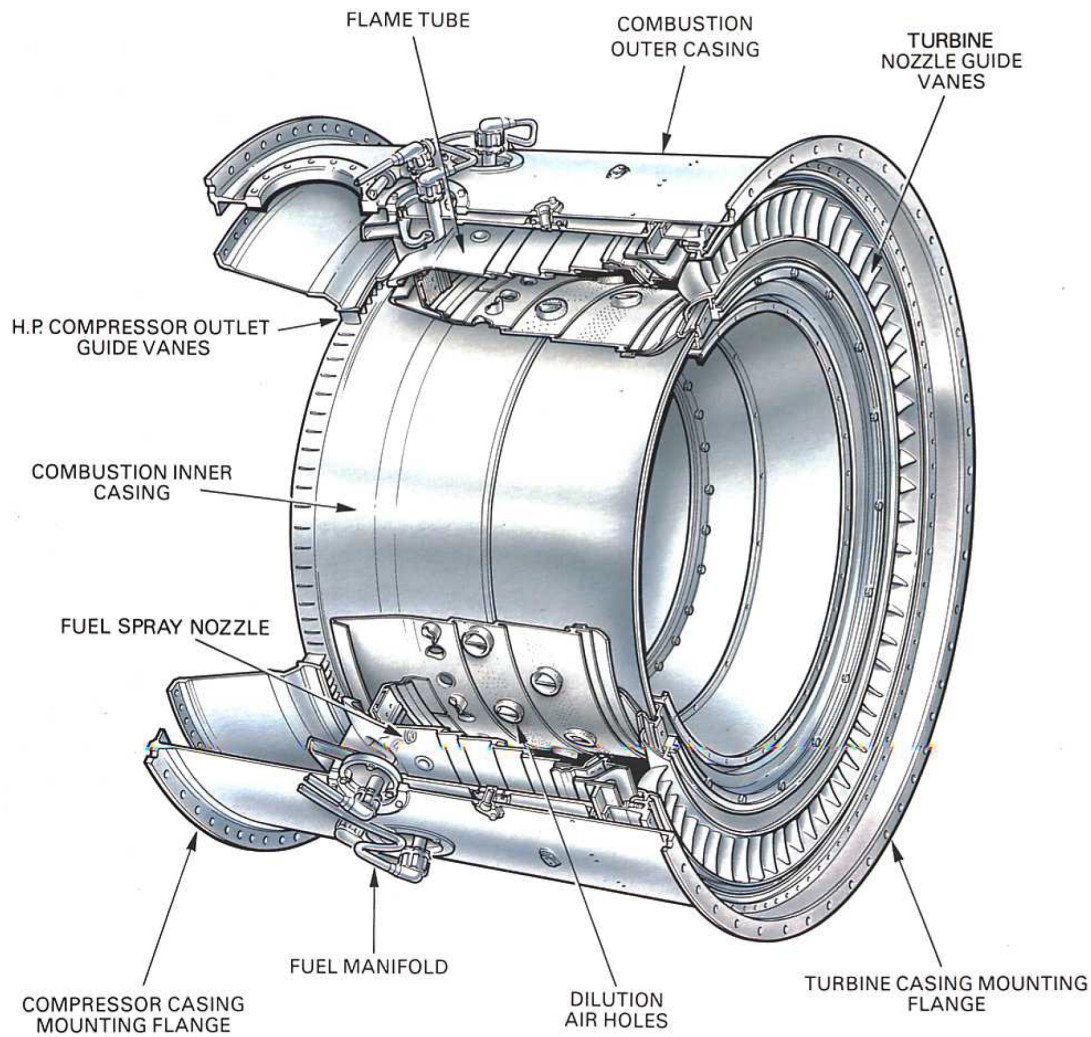
Figure 1.7: Annular combustor [2]

Fuel spray nozzles

Fuel spray nozzles have a function of distributing the fuel into the chamber. They're designed in a way to enhance the liquid atomization process, ensuring its rapid vaporization and burning. Atomizing spray nozzles have been developed into five distinct types:

- Simplex,

- variable port (Lubbock),

- Duplex or Duple,

- spill type,

- airspray nozzle [2].

The Simplex type, shown in Figure 1.8a, was used in early jet engines. It consists of a swirl chamber and a fixed-area atomizing orifice. This fuel spray nozzle performs differently, depending on the pressure drop across it. At higher fuel pressures, it performs satisfactory, but at the low pressures, examples being low engine speeds or high altitudes, the performance is inadequate.

Figure 1.8b shows the variable port, or Lubbock fuel spray nozzle which utilizes a spring-loaded piston to control the area of the inlet ports to the swirl chamber, eliminating the disadvantage of Simplex spray nozzles. At the same time, this design introduced problems in terms of balancing sets of spray nozzles as well as reliability issues (piston jamming due to dirt), the reason these type of fuel spray nozzles are not in use anymore.

The Duplex or Duple fuel spray nozzle, Figure 1.8c, embodies two independent orifices different in size, each having their own manifold. The smaller orifice handles lower pressure flows and the larger orifice deals with higher fuel pressures.

The spill type fuel spray nozzle is essentially a Simplex spray nozzle with a passage from the swirl chamber for fuel spillage. The fuel is constantly delivered to the nozzle at high pressure and the passage spills fuel away from the orifice in case of lower fuel demand. It is somewhat more complex system than the aforementioned, as special means for controlling, draining and recirculating the spill have to be provided.

The airspray nozzle, shown in Figure 1.8d, uses a proportion of the primary combustion air to intensify the atomization and improve air-fuel mixing. This fuel nozzle mitigates local fuel-rich concentrations, leading to reduction in carbon formation and exhaust smoke. Furthermore, the lower pressures required for atomization enable reduction in size, and consequently in weight, of the fuel pump.
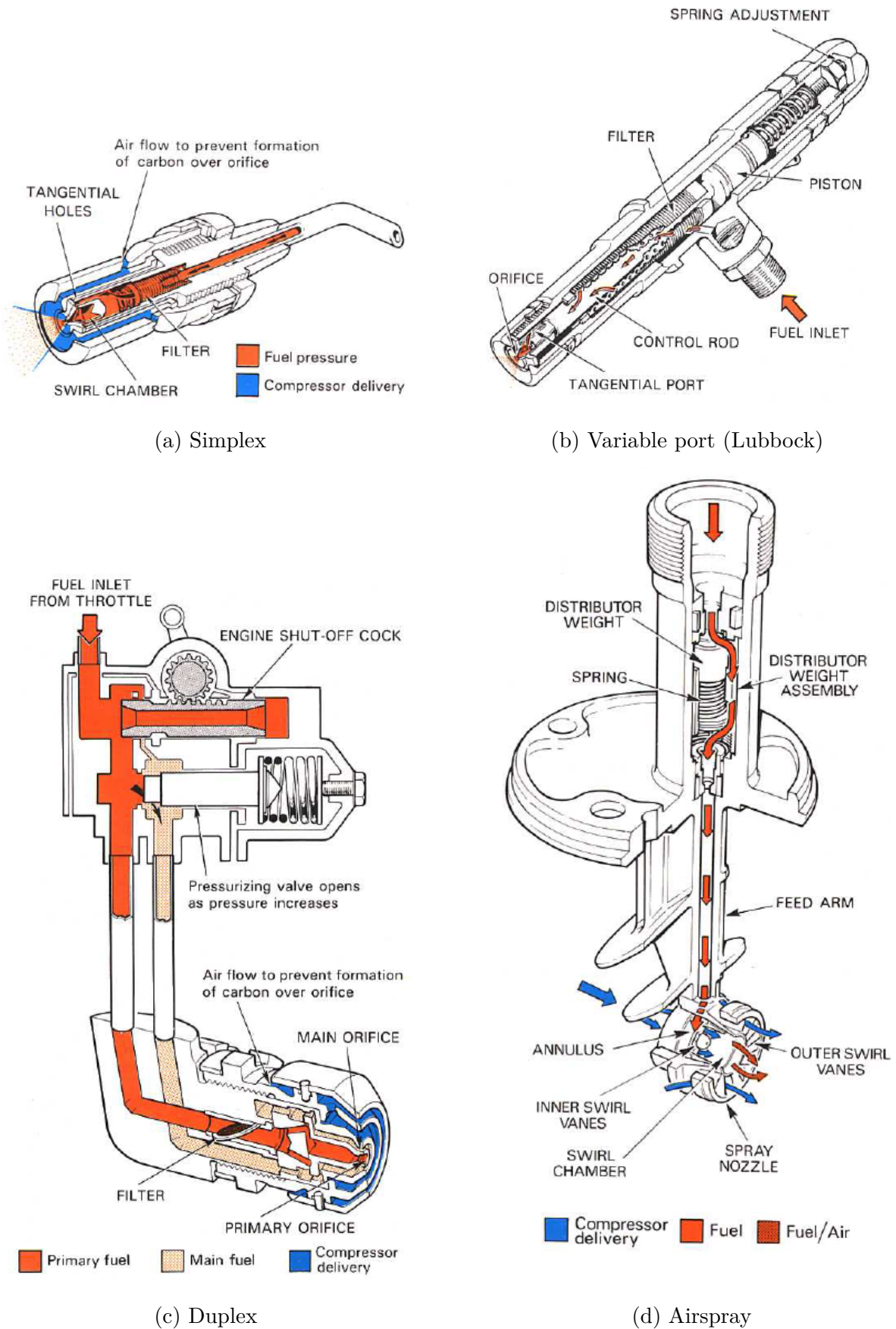
(a) Simplex

(b) Variable port (Lubbock)

(c) Duplex

(d) Airspray

Figure 1.8: Types of fuel spray nozzles [2]

1.1.3.   Expansion

After addition of energy from the combustion chamber, the gas undergoes expansion in the turbine and the nozzle. Throughout this process, the thermal and pressure energy are transformed into work, which drives the compressor, and the kinetic energy used for thrust.

Turbine

The turbine powers the compressor (and fan) by extracting energy from the gas and transforming it into work. Radial turbines, unlike their centrifugal compressor counterparts, are not used in jet engines, apart from the earliest models. Axial turbines are capable of providing better thermal management of hot exhaust gasses, which is the biggest challenge in the design process of turbine blades. Also, the number of turbine stages is lower compared to the axial compressor as the flow moves in the direction of decreasing pressure.

Nozzle

In turbojet engines, the entire thrust is generated in the nozzle by accelerating gas towards the nozzle outlet. Nozzles can be convergent or convergent-divergent. Convergent are used when the exiting flow is subsonic; they are easier to design, but suffer from efficiency losses since the pressure at the nozzle exit is higher than the ambient pressure.

Convergent-divergent nozzles, on the other hand, are capable of providing higher thrust at the expense of complexity. Flow accelerates through the converging part of the nozzle until reaching Ma=1 in the critical area - the throat of the nozzle. The nozzle diverges to allow further pressure decrease and acceleration of the supersonic flow. They are more complex to design and manufacture due to being variable-geometry. Figure 1.9 shows the two types of nozzles used in jet engines.
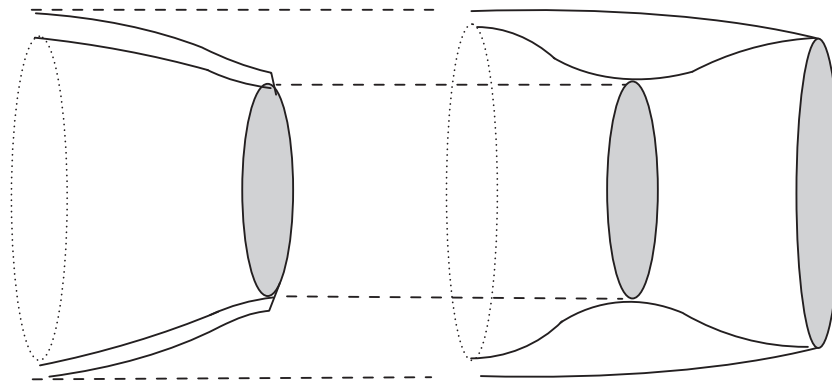
Figure 1.9: Convergent (left) and convergent-divergent nozzle (right) [1]

Afterburner

Some aircraft, mainly military supersonic, employ afterburners to increase thrust for short periods. Afterburning consists of the introduction and burning of fuel between the engine turbine and the nozzle, utilizing the unburned oxygen in the exhaust gas to support combustion. The resultant increase in the heat energy of the exhaust gas gives the increased kinetic energy of the jet leaving the propelling nozzle and therefore increases the engine thrust [2].

1.2.   Jet Fuels

While the oxidant for airbreathing jet engines is the compressed ambient air, there is a number of different fuels. Most jet engine fuels consist of complex mixtures of hundreds (if not thousands) of hydrocarbon species [3]. The following section will give an insight into some of the fuels used for airbreathing jet engines. Two types of jet fuels were most used throughout the history: the first being kerosene-type fuels and the second "wide-cut" fuel, which is basically a mixture of kerosene and gasoline. However, compared to a kerosene-type fuel, wide-cut jet fuel was found to have operational disadvantages due to its higher volatility [4]:

- greater losses due to evaporation at high altitudes,

- greater risk of fire during handling on the ground and

- crashes of planes fueled with wide-cut fuel were less survivable.

For that reason, kerosene-type fuels predominate in the world [4]. In U.S. designations, Jet A and Jet A-1 are standard commercial aircraft kerosene-type jet fuels. Most of the world uses Jet A-1, while Jet A is used in the U.S. The important difference between the two fuels is that Jet A-1 has a lower maximum freezing point than Jet A (Jet A: –40 °C, Jet A-1: –47 °C), making Jet A-1 more suitable for long international flights, especially on polar routes during the winter [4]. Wide-cut jet fuel, designated as Jet B, has even lower freezing point (around -62 °C) and for that reason it is still used in some extremely cold areas, like parts of Canada and Alaska [4].

Commercial aircrft jet fuels have their military counterparts. The U.S. military fuels designated as JP-8 and JP-4, where JP stands for "Jet Propellant", are equivalent to Jet A-1 and Jet B, respectively [1]. JP-8 is essentially Jet A-1, with three additives: a lubricity improver/corrosion inhibitor, an antistatic additive, and a fuel system icing inhibitor [5].

Less common are specialty fuels like JP-7, JP-TS and JP-10. JP-7 was originally developed for SR-71 Blackbird's Pratt & Whitney J58 engines. Its low volatility and high operational stability of roughly 288 °C (comparing with 163 °C for Jet A/Jet A-1) allowed it to be used as a coolant for SR-71's structure [6]. In more recent years, this fuel has been used to propel the scramjet experimental aircraft X-51 Wavereader [7]. JP-TS is almost exclusively used for U-2 reconnisance plane, with both good thermal stability of approx. 219 °C and maximum freezing point of -53 °C. JP-10 is a high-energy density fuel with a low freezing point (-79 °C), used in airbreathing cruise missiles [8]. Unlike previously referenced fuels, it is a single-component fuel, making it easier to model for research purposes. Downside of specialty fuels is the higher price than conventional fuels due to more complex manufacturing processes (JP-7 and JP-TS are roughly three times the cost of JP-8 [6]).

An alternative to petroleum-based aviation fuels are biofuels. The important advantages of renewable feedstock over petroleum include: sustainability, carbon dioxide recycling, renewability, eco-friendly technology and less dependence on petroleum supplying countries [9]. American Society of Testing and Materials (ASTM) has certified Fisher Tropsch (FT) fuels and hydroprocess edesters and fatty acids (HEFA) fuels for commercial purposes in up to 50% blends with standard jet fuels [10]. FT are hydrocarbon-based

fuels produced by a catalytic conversion of Syngas (CO and H_2) [11]. HEFA jet fuels are produced by the hydrodeoxygenation of vegetable oils, animal fats, waste grease, algal oil and bio-oil and the major side products are water and propane [9]. Biofuels have been used by airliners mostly for research studies. High production costs, limited availability and lack of policy incentives are presenting some of obstacles to widespread use [10].

More types of airbreathing jet fuels are available, most of them being either obsolete or in limited use. Some of the most important physical properties for fuels mentioned in this section are provided in Table 1.1.

Table 1.1: Typical propellants for airbreathing jet engines [1, 6, 8]

Fuel	Chemical formula	q_m [MJ/kg]	q_v [MJ/l]	ρ [kg/m^3]	Freezing point[b] [°C]	Flash point [°C]	Boiling points [°C]
Jet A	$C_{12.5}H_{24.2}$[a]	43.02	35.3	820	-40	38	150-300
Jet A-1 (JP-8)	$C_{12.5}H_{24.2}$[a]	43.4	34.7	800	-47	38	150-300
Jet B (JP-4)	$C_{10}H_{20.3}$[a]	43.6	33.1	760	-62	-23	73-280
JP-7	$C_{12.1}H_{24.4}$[a]	43.5	34.8	800	-30	60	182-288
JP-10	$C_{10}H_{16}$	42.1	39.6	940	-79	53	187

[a] approximation

[b] minimum

1.3. Numerical Modeling of the Combustion Process

Combustion modeling in jet engines represents a modern-day engineering challenge, describing the phenomena such as multiphase flows, jet atomization, turbulence, chemical kinetics, and others. The multiphase flow originates from the spray process of a fuel nozzle and there are a number of approaches to model it, e.g., Volume-of-Fluid (VOF), Euler

Lagrangian Discrete Droplet Method (DDM), Euler Eulerian multiphase approach, or a coupling of aforementioned approaches [12–14].

In most cases, chemical reactions occur on time scales comparable to other processes like diffusion, heat conduction and flow [15]. Laws of chemical kinetics provide information on the rate of chemical reactions. To successfully describe a fuel reaction process, an appropriate chemical mechanism has to be utilized. General Gas Phase Reactions (GGPR) of detailed chemical mechanisms contain a rather large number of chemical species and elementary reactions, but on the other hand, they are experimentally validated and applicable over a wide set of conditions [3]. An example of a detailed mechanism for the synthetic aviation fuel JP-10 is available in [16]. It is, in fact, one of the simplest detailed mechanisms for aviation fuels, constructed of 36 chemical species with 147 elementary reactions.

However, as kerosene type fuels are complex mixtures, simulating combustion of their exact composition is hardly possible [17]. To overcome that difficulty, fuel surrogates are introduced. A surrogate should be comprised of only a handful of components but be capable of emulating the gas phase combustion characteristics of the real fuel [18]. Aviation fuel surrogates have extensively been researched both experimentally and numerically, providing satisfactory results [19, 20]. Regardless of being simplified, detailed chemical kinetics mechanisms of surrogates are still computationally demanding for CFD codes as each species institutes supplementary partial differential equation to solve. Additionally, for turbulent flows, turbulence-chemistry interaction models have to be included [21–23]. As an illustration, a detailed reaction mechanism of a two component surrogate, containing 80% n-decane and 20% 1,2,4-trimethylbenzene by weight (named "Aachen" surrogate), that reproduces kerosene type fuels incorporates 122 species and 900 elementary reactions [24]. Even more complex reaction mechanisms are available, such as Jet-A POSF 4658 surrogate proposed in [18], constructed from the n-decane, iso-octane and toluene mixture with a total of 1607 species.

To incorporate combustion phenomena in practical engineering applications, detailed reaction mechanisms have to be reduced. One approach is optimizing detailed mechanisms by filtering out species and elementary reactions whose contribution to the combustion is minimal. Those reduced mechanisms typically contain a few dozen of species (or less) and hundreds of elementary reactions for kerosene type fuels, examples being

[25] with six mechanisms consisted of 10 to 25 species, and [26] with two mechanisms of 33 and 40 species respectively. Although reduced mechanisms decrease computational time, the accuracy is inevitably lost, making them usable only for particular intervals of conditions, i.e., pressures, temperatures, equivalence ratios, etc. The simplest mechanisms take into account only a single, global reaction; however, such mechanisms provide limited amount data, mainly useful for global studies.

Another acceleration method for chemistry is the Flamelet-Generated Manifold - (FGM) [27], based on a statement that a multidimensional flame can be constructed from an array of 1D flamelets, composed together in a tabulated manifold. The approach consists of a production of low dimensional look-up tables from a detailed reaction mechanism that can be read and used by the CFD code. Decreases in computational times of detailed reaction mechanisms with the FGM are substantial, making it appealing to further research.

2 | Mathematical Model

The next chapter will describe, in some detail, mathematical models relevant to the thesis. First, the fundamental conservation equations used in the finite volume method are shown. Turbulence modeling is presented afterwards, with the focus on the k-ζ-f model. Furthermore, the concept of multiphase flows is introduced, emphasizing the Euler Lagrangian approach for spray modeling along with its submodels. Finally, chemistry modeling is explained, providing information on chemical kinetics, employment of the Flamelet-Generated Manifold approach and details of the reaction mechanism.

2.1. Conservation Laws

A general definition for the conservation of physical flow properties can be explained as the following: the temporal change of the property within a control volume is equal to the sum of the surface flux of the property through the control volume boundaries and property creation or destruction within the control volume. This statement can be written in a form of the general conservation equation [28], also known as the general transport equation, describing the transport of an arbitrary scalar value φ:

$$\frac{\partial}{\partial t}\left(\rho\varphi\right) + \frac{\partial}{\partial x_j}\left(\rho\varphi u_j\right) = \frac{\partial}{\partial x_j}\left(\Gamma_\varphi \frac{\partial\varphi}{\partial x_j}\right) + S_\varphi. \tag{2.1}$$

The first term is the unsteady term and the second term is the convective term, representing the convective transport of the scalar property by a convective velocity u_j. The third term is the diffusion term containing the diffusion coefficient Γ_φ. The last term is the source/sink term. The governing equations of the fluid flow as well as the chemical species transport can be derived from the equation above.

2.1.1.   Mass conservation

The mass conservation, or the continuity equation derives from the general transport equation by setting φ to 1. Mass is not transported by diffusion and the mass can not be formed nor destroyed, thus the diffusion and source terms are absent. Hence, the expression for the mass conservation in the conservative (flux) form is defined as:

$$\frac{\partial \rho}{\partial t} + \frac{\partial}{\partial x_j}\left(\rho u_j\right) = 0 \tag{2.2}$$

2.1.2.   Momentum conservation

The momentum conservation law (Newton's second law) states that the sum of the volume and surface forces acting on a fluid control volume element is equal to the time rate of momentum change of the fluid control volume element. The momentum conservation can be written as

$$\frac{\partial}{\partial t}\left(\rho u_i\right) + \frac{\partial}{\partial x_j}\left(\rho u_j u_i\right) = \frac{\partial \sigma_{ji}}{\partial x_j} + f_i, \tag{2.3}$$

where σ_{ji} is the stress tensor, representing surface forces, whereas f_i are body forces. Surface forces can further be written as the combination of pressure and viscous stresses:

$$\sigma_{ji} = -p\delta_{ji} + \tau_{ji}, \tag{2.4}$$

For Newtonian fluids, the viscous stress tensor can be expressed as

$$\tau_{ji} = 2\mu D_{ji} - \frac{2}{3}\mu\frac{\partial v_k}{\partial x_k}\delta_{ji} \tag{2.5}$$

In the equation above, μ is the molecular viscosity coefficient and D_{ji} is the rate of strain (deformation) tensor:

$$D_{ji} = \frac{1}{2}\left(\frac{\partial v_j}{\partial x_i} + \frac{\partial v_i}{\partial x_j}\right). \tag{2.6}$$

Combining the Eq. (2.3-2.5) and defining the body force as the gravitational force (ρg_i) the most general form of Navier-Stokes equations for Newtonian fluids can be obtained:

$$\frac{\partial}{\partial t}(\rho u_i) + \frac{\partial}{\partial x_j}(\rho u_j u_i) = -\frac{\partial p}{\partial x_i} + \left(\frac{\partial v_j}{\partial x_i} + \frac{\partial v_i}{\partial x_j}\right) - \frac{2}{3}\mu\frac{\partial v_k}{\partial x_k}\delta_{ji} + \rho g_i. \tag{2.7}$$

2.1.3. Energy conservation

Energy conservation law is the the first law of thermodynamics. It states that the energy can not be created nor destroyed, it can be converted from one form to another. The equation can be written in the terms of specific total energy e, deriving from the general transport equation:

$$\frac{\partial}{\partial t}(\rho e) + \frac{\partial}{\partial x_j}(\rho u_j e) = \frac{\partial}{\partial x_j}(\sigma_{ji} u_i) + \rho g_i u_i - \frac{\partial q_i}{\partial x_i} + S_v \tag{2.8}$$

The first term represents the rate of the total energy change and the second term is the total energy transfer through the control volume boundaries. The net rate of work done by the control volume is due to surface and body forces, which is denoted by the first two terms on the right-hand side respectively. The net rate of heat transferred to the control volume is a sum of the surface transfer (heat flux, second term on the right-hand side) and created/destroyed heat (the last term on the right-hand side).

The specific total energy e is defined as the sum of internal and kinetic energies and can be written as

$$e = u_e + \frac{1}{2}u_j u_i. \tag{2.9}$$

The energy equation can also be written in terms of specific enthalpy, specific internal energy or in terms of temperature. The heat flux represents heat transfer by diffusion and it's governed by Fourier's law:

$$q_s = -\lambda\frac{\partial T}{\partial x_i} \tag{2.10}$$

where λ denotes the thermal conductivity coefficient.

2.1.4. Species mass conservation

A chemical species is an ensemble of chemically identical molecular entities that can explore the same set of molecular energy levels on the time scale of the experiment [29].

Transport properties of chemical species are of particular interest when dealing with reacting flows, as their creation and destruction are the basis of chemical reactions, such as combustion.

The species mass conservation equation [30], unlike the continuity equation, contains the source term as species can form or be destroyed through chemical reactions:

$$\frac{\partial}{\partial t}\left(\rho Y_i\right) + \frac{\partial}{\partial x_j}\left(\rho u_j Y_i\right) = \frac{\partial}{\partial x_j}\left(\Gamma_{Y_i}\frac{\partial Y_i}{\partial x_j}\right) + S_{Y_i},\tag{2.11}$$

In the equation above, Γ_{Y_i} can be expressed as

$$\Gamma_{Y_i} = \rho D_{i,m} + \frac{\mu_t}{S_{c_t}},\tag{2.12}$$

where $D_{i,m}$ stands for the mass diffusion coefficient for species i in the mixture and S_{C_t} is the turbulent Schmidt number with a default value of 0.7 [30]. Furthermore, in the Eq. (2.11) Y_i denotes the mass fraction of the i-th chemical species:

$$Y_i = \frac{m_i}{m}.\tag{2.13}$$

The mass source is defined as:

$$S_{Y_i} = \dot{r}_i \cdot M_i,\tag{2.14}$$

where $\dot{r}_i$ and M_i are reaction rate and molar mass of species i, respectively.

2.2.   Turbulence Modeling

The vast majority of flows in nature are turbulent. Whereas laminar flows are stable, turbulent flows are chaotic, diffusive causing rapid mixing, time-dependent, and involve three-dimensional vorticity fluctuations with a broad range of time and length scales [28, 31].

It is possible to directly solve the Navier-Stokes equations for turbulent flows by the means of Direct Numerical Simulations (DNS), or partially by employing Large Eddy Simulations (LES) where small turbulent scales are filtered and solved with a turbulence model. Even though they're becoming more frequent, those two approaches are still computationally too demanding to become a mainstream in industry [32].

The most widespread approach to solving turbulent flows is by employing the Reynolds Averaged Navier-Stokes (RANS) equations which are statistically derived, time-averaged equations whose goal is to model all scales of turbulence. They are based on Reynolds decomposition in which physical quantities are decomposed into a mean value and a fluctuating component. Reynolds averaging introduce non-linear terms into Naver-Stokes equations which are then treated by means of turbulence models. This thesis uses the $k - \zeta - f$ turbulence model, which is explained in detail in the following section.

2.2.1.   The $k - \zeta - f$ turbulence model

The $k - \zeta - f$ is an eddy-viscosity turbulence model [33], proposed as a modification of $\overline{v^2} - f$ model [34], with the aim of improving the numerical stability of the original model. The eddy-viscosity is obtained from:

$$\nu_t = C_\mu \zeta \frac{k^2}{\epsilon}, \tag{2.15}$$

where C_μ is the model constant, k is the turbulent kinetic energy, ϵ is the turbulent kinetic energy dissipation rate and ζ is the velocity scale ratio:

$$\zeta = \frac{\overline{v^2}}{k}. \tag{2.16}$$

The rest of the variables are obtained from the following set of equations:

$$\rho \frac{Dk}{Dt} = \rho \left(P_k - \epsilon \right) + \frac{\partial}{\partial x_j} \left[\left(\mu \frac{\mu_t}{\sigma_k} \right) \frac{\partial k}{\partial x_j} \right]$$

$$\rho \frac{D\epsilon}{Dt} = \rho \frac{C_{\epsilon 1}^* P_k - C_{\epsilon 2} \epsilon}{T} + \frac{\partial}{\partial x_j} \left[\left(\mu \frac{\mu_t}{\sigma_k} \right) \frac{\partial k}{\partial x_j} \right] \tag{2.17}$$

$$\rho \frac{D\zeta}{Dt} = \rho f - \rho \frac{\zeta}{k} P_k + + \frac{\partial}{\partial x_j} \left[\left(\mu \frac{\mu_t}{\sigma_k} \right) \frac{\partial k}{\partial x_j} \right],$$

where the following form of the f equations is adopted

$$f - L^2 = \frac{\partial^2 f}{\partial x_j \delta x_j} = \left(C_1 + C_2 \frac{P_k}{\zeta} \right) \frac{(2/3 - \zeta)}{T}. \tag{2.18}$$

The turbulent time scale T and length scale L are expressed as

$$T = \max\left(\min\left(\frac{k}{\epsilon}, \frac{a}{\sqrt{6}C_\mu |S|\zeta}\right), C_T \left(\frac{\nu}{\epsilon}\right)^{\frac{1}{2}}\right)$$
$$L = \max\left(\min\left(\frac{k^{\frac{3}{2}}}{\epsilon}, \frac{k^{\frac{1}{2}}}{\sqrt{6}C_\mu |S|\zeta}\right), C_\eta \frac{\nu^{\frac{3}{4}}}{\epsilon^{\frac{1}{4}}}\right) \tag{2.19}$$

The ϵ equation constant $C_{\epsilon 1}$ is dampened close to the wall, thus the modification is introduced:

$$C_{\epsilon 1}^* = C_{\epsilon 1}\left(1 + 0.0045\sqrt{\frac{1}{\zeta}}\right). \tag{2.20}$$

Model constants in Eqs. (2.15) to (2.20) are determined empirically, and they're set to recommended values [33], as shown in Table 2.1.

Table 2.1: $k - \zeta - f$ model coefficients tuned to generic flows

C_μ	$C_{\epsilon 1}$	$C_{\epsilon 2}$	C_1	C_2	σ_k	σ_ϵ	σ_ζ	C_L	C_η	C_τ
0.22	$1.4\left(1 + 0.012/\zeta\right)$	1.9	0.4	0.65	1	1.3	1.2	6	0.36	85

2.3. Multiphase Flows

Multiphase flows are flows consisting of more than one phase or component on a scale above the molecular level. An example of multiphase flow would be a flow of different states of matter or a flow with distinct boundary between components (eg. water-oil mixture). Another example is present in the jet engine combustion chamber, where the the liquid fuel is injected into the ambient air. Furthermore, two general topologies of multiphase flow can be identified: dispersed (diluted) flows and separated (dense) flows. Dispersed flows are consisted of finite particles, drops or bubbles distributed in a volume of the connected phase, whereas separated flows consist of two or more continuous phases separated by interfaces [35]. None of the existing models are able the capture the multiphase phenomena entirely. Hence, advantages and disadvantages of each model has to be taken into account when solving a certain problem.

The most established approach for solving the fuel injector spray process is the Euler-Lagrangian Discrete Droplet Method (DDM) which calculates trajectories, as well as the

mass, momentum and heat transfer of individual particles.

2.3.1.   Euler Lagrangian DDM

In the Euler Lagrangian DDM, individual droplets, similar in dimensions and physical quantities, are grouped together in so-called parcels and tracked through the domain using the Lagrangian formulation. The gas phase is described using the Eulerian formulation. The phase coupling is performed by introducing the source terms for mass, momentum and energy exchange. In the transport equations, the trajectory and velocity of a parcel is derived from the Newton's Second Law of motion:

$$m_p \frac{du_{id}}{dt} = \sum F_i, \tag{2.21}$$

where m_p is the parcel mass and $\sum F_i$ is the sum of all forces acting upon the parcel.

To adequately capture the spray phenomena, several sub-models are introduced, such as the primary and secondary breakup, evaporation, droplet deformation, collision and coalescence and turbulent dispersion. These submodels enable appropriate handling of physical processes that would otherwise not be covered by the general transport equations [36]. Following sections will present submodels used in the thesis.

The computational effort for this approach increases noticeably with increasing parcel number, making its primary application for sufficiently diluted spray where the volume fraction of the liquid phase is relatively low [21].

WAVE breakup

The WAVE breakup model predicts breakup resulting from the action of different combinations of liquid inertia, surface tension and aerodynamic forces on the jet, producing drops of different sizes than the parent drop sizes [37]. The model assumes that the time of breakup and the resulting droplet size are related to the fastest-growing Kelvin-Helmholtz instability.

The rate of radius reduction of the parent drops is expressed as

$$\frac{dr}{dt} = -\frac{r - r_{\text{stable}}}{\tau_a}, \tag{2.22}$$

with r_{stable} representing the product droplet radius and τ_a denoting the breakup time of

the model. The product droplet radius is expressed proportionally to the wavelength Λ of the fastest growing wave on the parcel surface:

$$r_{\text{stable}} = \Lambda \cdot C_1, \tag{2.23}$$

where C_1 is the WAVE model constant, with the recommended value of 0.61 [30]. The breakup time of the model is given by an expression:

$$\tau_a = \frac{3.726 \, C_2 \, r}{\Lambda \Omega}. \tag{2.24}$$

The second model constant C_2 serves as the characteristic breakup time correction and it varies from one injector to another. The wave length Λ and wave growth rate Ω are described with empirical relations, depending on the local flow properties:

$$
\begin{aligned}
\Lambda &= 9.02 \cdot r \, \frac{\left(1 + 0.45 \cdot Oh^{0.5}\right)\left(1 + 0.4 \cdot T^{0.7}\right)}{\left(1 + 0.87 \cdot We_g^{1.67}\right)^{0.6}} \\
\Omega &= \left(\frac{\rho_d \, r^3}{\sigma}\right)^{-0.5} \frac{0.34 + 0.38 \cdot We_g^{1.5}}{\left(1 + Oh\right)\left(1 + 1.4 \cdot T^{0.6}\right)}.
\end{aligned}
\tag{2.25}
$$

In the equation above, σ is the surface tension and We and Oh are Weber and Ohnesorge numbers respectively, defined as:

$$
\begin{aligned}
We &= \frac{2r\rho u^2}{\sigma} \\
Oh &= \frac{\mu}{\sqrt{2r\rho\sigma}} = \frac{\sqrt{We}}{Re},
\end{aligned}
\tag{2.26}
$$

as well as $T = Oh \, We^{0.5}$.

Abramzon and Sirignano evaporation model

The Abramzon and Sirignano evaporation model [38] is based on the classic film theory where the resistances to heat and mass transfer are modeled by fictional gas films of constant thickness, δ_T and δ_M:

$$
\begin{aligned}
\delta_T &= \frac{2r_s}{Nu_0 - 2} \\
\delta_M &= \frac{2r_s}{Sh_0 - 2},
\end{aligned}
\tag{2.27}
$$

where Nu_0 is the Nusselt number derived for non-evaporating droplets, and Sh_0 is the analogous Sherwood number:

$$Nu_0 = 2 + 0.552 Re^{1/2} Pr^{1/3}$$
$$Sh_0 = 2 + 0.552 Re^{1/2} Sc^{1/3}.$$

(2.28)

These film thicknesses are corrected with factors F_T and F_M for an evaporating droplet. The droplet evaporation rate can be calculated according to the following expression:

$$\dot{m} = \pi \overline{\rho_g} \overline{\beta_g} D_d Sh^* \ln\left(1 + B_M\right)$$
$$\dot{m} = \pi \frac{\overline{k_g}}{c_{pF}} D_d Nu^* \ln\left(1 + B_T\right).$$

(2.29)

In the equation above, terms $\overline{\rho_g}$, $\overline{\beta_g}$ and $\overline{k_g}$ are average density, binary diffusion coefficient, thermal conductivity of the gas mixture, and $\overline{C_{pF}}$ is the average vapor specific heat in the film. The modified Nusselt and Sherwood numbers are defined as the non-dimensional heat and mass transfer coefficients according to:

$$Sh^* = 2 + \frac{Sh_0 - 2}{F_M}$$
$$Nu^* = 2 + \frac{Nu_0 - 2}{F_T}.$$

(2.30)

The values B_M and B_T are known as the Spalding mass and heat transfer numbers and they're given as:

$$B_M = \frac{Y_{F_s} - Y_{F_\infty}}{1 - Y_{F_s}}$$
$$B_T = \frac{\overline{C_{pF}}\left(T_\infty - T_S\right)}{L\left(T_S\right) + \frac{Q_L}{m}}.$$

(2.31)

In the expression above, Y_F is the fuel mass fraction and $L(T_S)$ is the latent heat of vaporization at the temperature (T_S). Subscripts s and ∞ refer to conditions at the droplet surface and external gas flow.

Turbulent dispersion

It is assumed that turbulent eddies interact with fluid particles in the flow by deflecting them, thus altering their trajectories. A turbulent dispersion model is used to describe the particle-turbulence interaction as they can not be resolved by the flow field in detail.

In this thesis, the stochastic dispersion method presented in [39] is employed. The model includes the effects of turbulence on the spray particles by adding a fluctuating velocity u_i. The fluctuating velocity is determined randomly from a Gaussian distribution with standard deviation $\sigma = \sqrt{\frac{2}{3}k}$:

$$u_i' = \sqrt{\frac{2}{3}k} \cdot \mathrm{sign}\left(2\mathrm{Rn}_i - 1\right) \cdot \mathrm{erf}^{-1}\left(2\mathrm{Rn}_i - 1\right), \tag{2.32}$$

where k is the turbulence kinetic energy of the gas at the particle location, Rn is a random number in the range from $[0 < \mathrm{Rn}_i < 1]$ for each vector component and erf^{-1} is the inverse Gauss function.

The fluctuation velocity is determined as a constant function of time and is updated when the turbulence correlation time has passed. The turbulence correlation time is the minimum of the eddy break-up time and the time for the particle to pass over an eddy:

$$t_{\mathrm{turb}} = \min\left(C_\tau \frac{k}{\epsilon}, \, C_1 \frac{k^{3/2}}{\epsilon} \frac{1}{|u_g + u' - u_d|}\right). \tag{2.33}$$

In the equation above, $C_\tau = 1$ and $C_1 = 0.16532$ are model constants. In case that the computational time step is larger than the turbulence correlation time, the spray integration time step is reduced to t_{turb}.

2.4.   Chemistry Modeling

As stated in Section 1.3., chemistry of the combustion process can be described by solving General Gas Phase Reactions (GGPR) of the computationally demanding detailed chemical mechanism or by employing one of reduced reaction mechanisms which are limited to a specific purpose. Chemical mechanism is described with elementary chemical reactions of chemical species. The source terms accounting for the gas phase reactions in the species transport equations and in the gas phase energy equation are calculated with reaction rates depending on species concentrations and temperature. The general form of corresponding reaction rates is

$$\sum_{k=1}^{K} \nu_{ki}' \cdot \kappa_k \Leftrightarrow \sum_{k=1}^{K} \nu_{ki}'' \quad (i = 1, ..., I), \tag{2.34}$$

where ν are stoichiometric coefficients and κ is the chemical symbol for the kth species. K represents the total number of gas phase species in the system and I is the total number of chemical reactions considered. Eq.(2.34) is valid for both reversible and irreversible reactions. The forward reaction rate constant can be expressed through the empirical Arrhenius law [15]:

$$k_{\text{f}} = A\,T^{b} \cdot \exp\left(-\frac{E_a}{RT}\right).$$ (2.35)

In the equation above, A and b are equation coefficients, and E_a is the activation energy. All three terms are determined experimentally and are unique for an associated elementary reaction. Realistic kinetic models must adhere strictly to those rate expressions which have been measured experimentally, within their stated uncertainty limits [40]. For reversible reactions, the backward reaction rate is the ratio of the forward reaction rate and equilibrium constant:

$$k_{\text{b}_i} = \frac{k_{\text{f}_i}}{K_{\text{c}_i}}.$$ (2.36)

The equilibrium constant can be expressed as

$$K_{\text{c}_i} = \prod_{k=1}^{K} [c_k]^{\left(\nu'_{ki} - \nu''_{ki}\right)},$$ (2.37)

in which c_k denotes the molar concentration. The rate of the reaction S_{Y_k} for k^{th} species is defined by an expression

$$S_{Y_k} = W_k \sum_{i=1}^{K} \left(\nu''_{ki} - \nu'_{ki}\right) \left[k_{\text{f}_i} \prod_{k=1}^{K} [c_k]^{\nu'_{ki}} - k_{\text{b}_i} \prod_{k=1}^{K} [c_k]^{\nu''_{ki}} \right].$$ (2.38)

W_k from the expression above denotes the molecular weight and S_{Y_k} represents the source term from the Eq.(2.11).

A number of species for a detailed aviation fuel mechanism, as seen in the literature review, can be as much as a couple of hundreds, or more. Each additional species consequently adds additional transport equation to solve, making detailed chemical mechanism GGPR computationally demanding. Nonetheless, chemistry solution can be accelerated by using the tabulated chemistry approach, e.g., the Flamelet-Generated Manifold, which is illustrated in the next section.

2.4.1.   Flamelet-Generated Manifold based combustion model

The Flamelet-Generated Manifold (FGM) method allows a noticeable speed-up of CFD with detailed chemistry. It is based on a combination of two approaches which simplify flame calculations - the flamelet approach and the manifold approach [27]. The FGM method shares the assumption with flamelet approaches that a multi-dimensional flame may be considered as an ensemble of one-dimensional flames [27]. The implementation, however, is typical for a manifold method, which means that the reaction rates and other essential variables are stored in a look-up table and are used to solve conservation equations for the controlling variables [27]. The AVL TABKIN™ FGM combustion model implements the detailed chemistry tabulation into the framework of AVL FIRE™ CFD code [30]. It is based on a progress variable/mixture fraction approach.

The look-up tables are derived from a detailed chemical mechanism, they're based on ignition homogeneous reactor chemistry calculations and have up to 8 dimensions:

- pressure,

- fresh gas temperature,

- mixture fraction and its variance,

- progress variable and its variance,

- exhaust gas recirculation (EGR) and

- fuel composition parameter.

The mixture fraction is a conserved scalar which determines the fuel/air mixing. It has the following properties relevant to liquid fuels:

- is zero in the oxidizer and unity in fuel;

- is not consumed by the reaction;

- is equal to the fuel in the non-reacting case;

- has a spray source term for liquid fuels.

The mean mixture fraction equation reads as follows:

$$\frac{\partial}{\partial t}\left(\bar{\rho}\widetilde{Z}\right) + \frac{\partial}{\partial x_i}\left(\bar{\rho}\widetilde{u}_i\widetilde{Z}\right) = \frac{\partial}{\partial x_i}\left(\bar{\rho}\left(D + D_T\right)\frac{\partial \widetilde{Z}}{\partial x_i}\right) + \bar{\widetilde{S}}_{vap}. \tag{2.39}$$

The mean mixture fraction variance equation is expressed as

$$\frac{\partial}{\partial t}\left(\bar{\rho}\widetilde{Z''^2}\right) + \frac{\partial}{\partial x_i}\left(\bar{\rho}\widetilde{u}_i\widetilde{Z''^2}\right) = \frac{\partial}{\partial x_i}\left(\bar{\rho}\left(D + D_T\right)\frac{\partial \widetilde{Z''^2}}{\partial x_i}\right) + 2\bar{\rho}D_T\left(\frac{\partial \widetilde{Z}}{\partial x_i}\right)^2 - \bar{\rho}\widetilde{\chi}_Z, \tag{2.40}$$

where the scalar dissipation rate $\widetilde{\chi}_Z$ is

$$\widetilde{\chi}_Z = 2\frac{\epsilon}{k}\widetilde{Z''^2}. \tag{2.41}$$

The progress variable is a scalar describing the advancement of the ignition and flame, i.e., the reaction progress from fresh to burnt gas. When normalized, it is zero in the fresh gas and unity in the burnt gas, and it has a source term from the chemistry. The progress variable is defined as a linear combination of species, for example if CO and CO_2 are in question:

$$Y_c = \frac{Y_{CO}}{W_{CO}} + \frac{Y_{CO_2}}{W_{CO_2}}. \tag{2.42}$$

The progress variable can be normalized:

$$c = \frac{Y_C}{Y_C^{EQ}}. \tag{2.43}$$

Then, the transport equation for the normalized mean progress variable and its variance can be written:

$$\frac{\partial}{\partial t}\left(\bar{\rho}\widetilde{c}\right) + \frac{\partial}{\partial x_i}\left(\bar{\rho}\widetilde{u}_i\widetilde{c}\right) = \frac{\partial}{\partial x_i}\left(\bar{\rho}\left(D + D_T\right)\frac{\partial \widetilde{c}}{\partial x_i}\right) + \bar{\widetilde{S}}_c, \tag{2.44}$$

$$\frac{\partial}{\partial t}\left(\bar{\rho}\widetilde{c''^2}\right) + \frac{\partial}{\partial x_i}\left(\bar{\rho}\widetilde{u}_i\widetilde{c''^2}\right) = \frac{\partial}{\partial x_i}\left(\bar{\rho}\left(D + D_T\right)\frac{\partial \widetilde{c''^2}}{\partial x_i}\right) + 2\bar{\rho}D_T\left(\frac{\partial \widetilde{c}}{\partial x_i}\right)^2 - \bar{\rho}\widetilde{\chi}_c, \tag{2.45}$$

with the scalar dissipation rate:

$$\widetilde{\chi}_c = 2\frac{\epsilon}{k}\widetilde{c''^2}. \tag{2.46}$$

The look-up tables enable reduction of the number of species to five, with the retention of correct thermochemistry. The used chemical species are O_2, CO_2, H_2O, N_2 and the last chemical species being the virtual fuel. The virtual fuel [41] allows imposing species mass fractions from the look-up table, thus comprising all combustible matter present in a real burning mixture. In addition, it burns in a single step. The rate of change of the virtual fuel mass fraction is computed using the expression

$$\dot{Y}_F = \frac{Y_{VF}\left(c\left(t + \Delta t\right),\, coords\right) - Y_{VF}\left(t\right)}{\Delta t},$$ (2.47)

where variable *coords* is denoting values (coordinates) from the look-up tables. The rate of change of other species of the virtual system are calculated by the CFD code, based on the stoichiometric coefficients. The total chemical heat source term is computed from species change rates and their partial enthalpies:

$$\dot{S}_{heat} = \rho \sum_{i=1}^{n} \dot{S}_i h_i.$$ (2.48)

2.4.2. Chemical kinetics mechanism

Chemical mechanism of JP-10 (chemical formula $C_{10}H_{16}$, molecule shown in Figure 2.1), previously mentioned in Section 1.3., was selected for combustion modeling due to simplicity. This chemistry mechanism is described with 174 elementary steps among 36 chemical species [16].
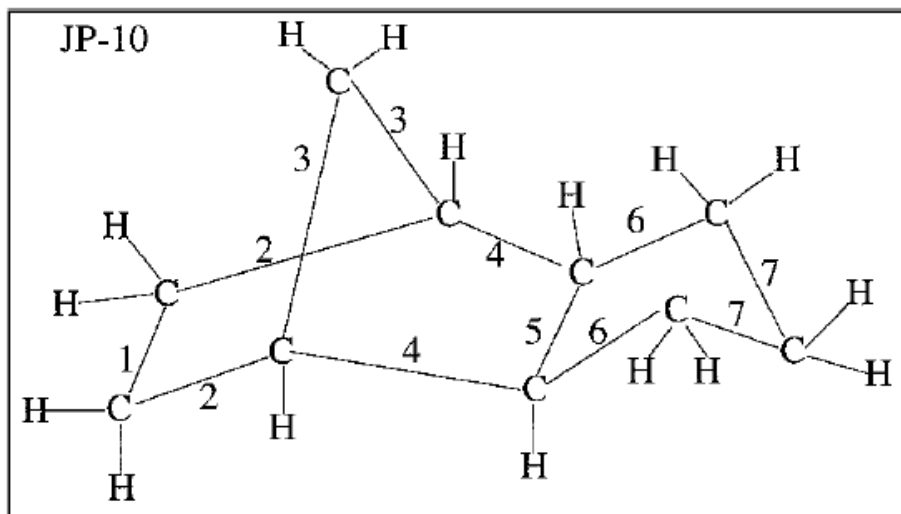
Figure 2.1: JP-10 molecule [16]

The first part of the mechanism is the chemistry of JP-10 breakdown through 27 irreversible elementary reactions to form smaller hydrocarbons containing no more than three carbon atoms ($C_1 - C_3$ species). The breakdown, along with specific reaction-rate constants of Eq. 2.35, is shown in Table A.1 in Appendix. The largest part of the mechanism is dedicated to reaction of C_1-C_3 species, specifically the other 147 elementary reactions.

The JP-10 mechanism was derived with the objective autoignition times for temperatures between 1000 and 2500 K, pressures between 1 and 100 bar, the typical range of conditions found in the propulsion applications. Even though it's a single-component fuel, JP-10 is still too large molecule for complete detailed description of its decomposition [16]. Therefore, the presented mechanism is based on a number of theoretical assumptions which introduce model limitations. The limitations include calculation of product distributions above C_3, results for equivalence ratios above 2 and predictions for temperatures below 1000 K.

3 | Numerical Setup

The following chapter will address the numerical setup of the can combustor case, formulated in the commercial software package AVL FIRE™ which specializes in the field of combustion analysis. Geometry of the combustor is shown, along with the computational mesh. Afterwards, the boundary and initial conditions are provided, as well as the spray setup. The next is the combustion setup, where employed chemistry solving approaches are described and combustion ignition data are given. As a final point, the simulation setup is given, providing the data on discretization schemes used, as well as convergence criteria and underrelaxation factors.

3.1. Combustor Geometry and Computational Mesh

The combustor is an artificial model of a can type combustor [42], consisted of a double stage radial swirler, single fuel nozzle and a liner without dilution holes. It has previously been used for qualitative analysis of spray formation, combustion and pollutant modeling [42, 43]. The most important dimensions of the combustor are shown in Figure 3.1, whilst the 3D model is shown in Figure 3.2.
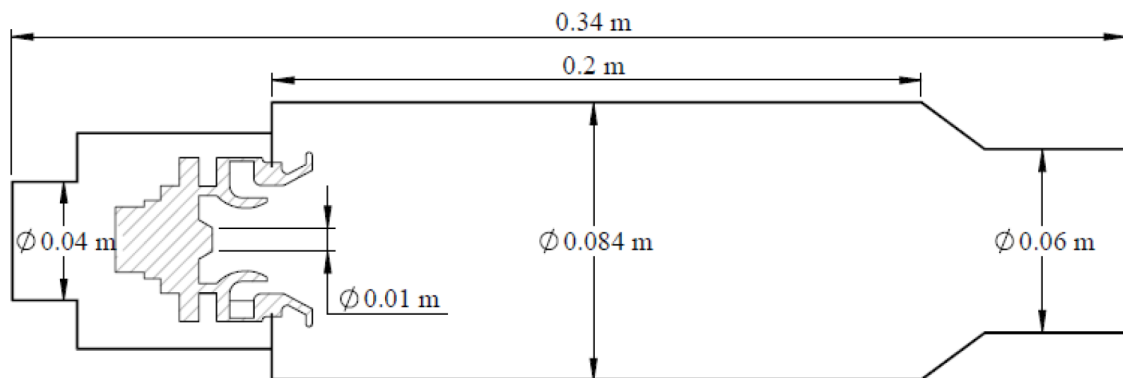
Figure 3.1: Combustor dimensions [43]
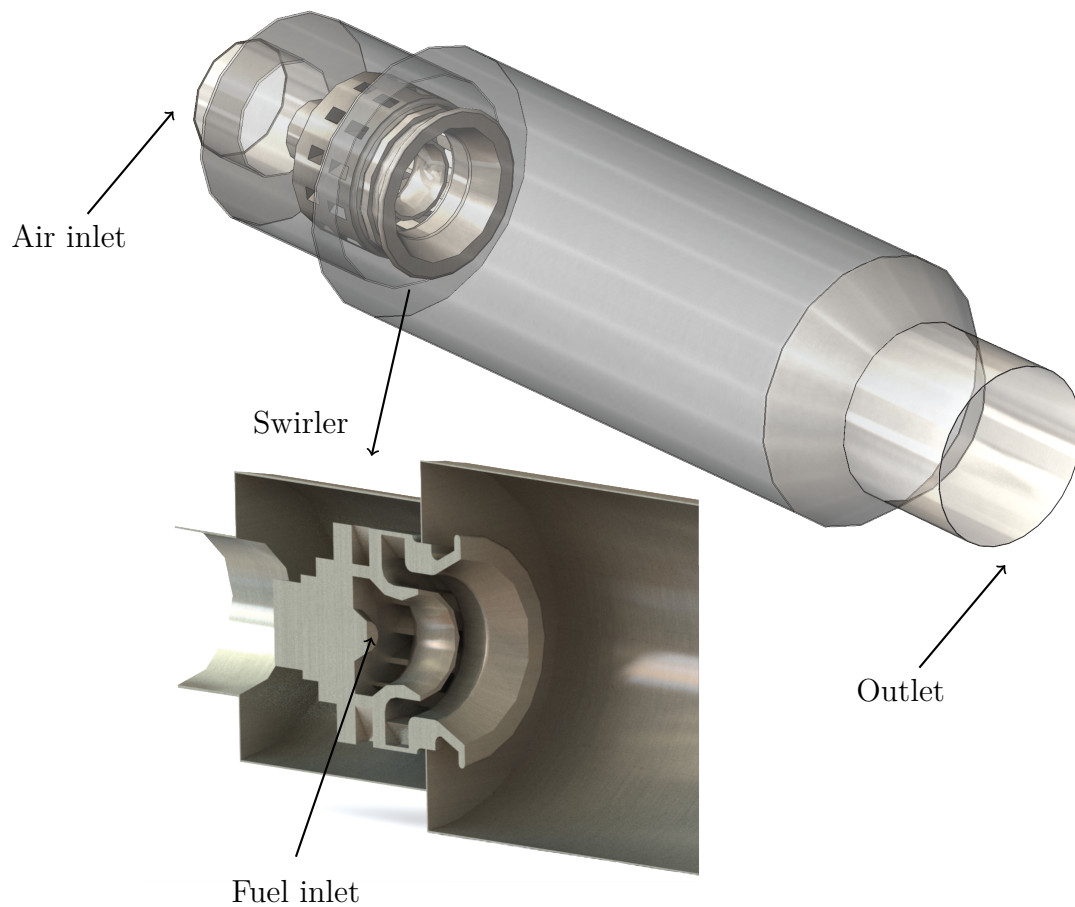
Figure 3.2: Combustor CAD model

Meshes were made using the FIRE automatic mesher. Three computational domains were generated for the mesh dependency test, with the total number of control volumes raging from approximately 335 000 to 700 000. Characteristic data for each mesh is presented in Table 3.1.

Table 3.1: Mesh dependency domain characterization

Mesh resolution	Minimum cell dimension [m]	Maximum cell dimension [m]	Total number of cells
Coarse	0.0008025	0.00321	336042
Medium	0.0006581	0.00263	460415
Fine	0.0005062	0.002025	701823

The most dependent structural element on the mesh resolution is the swirler, hence the most refinement can be observed in that particular area, as suggested in Figure 3.3.

a)   b)   c)
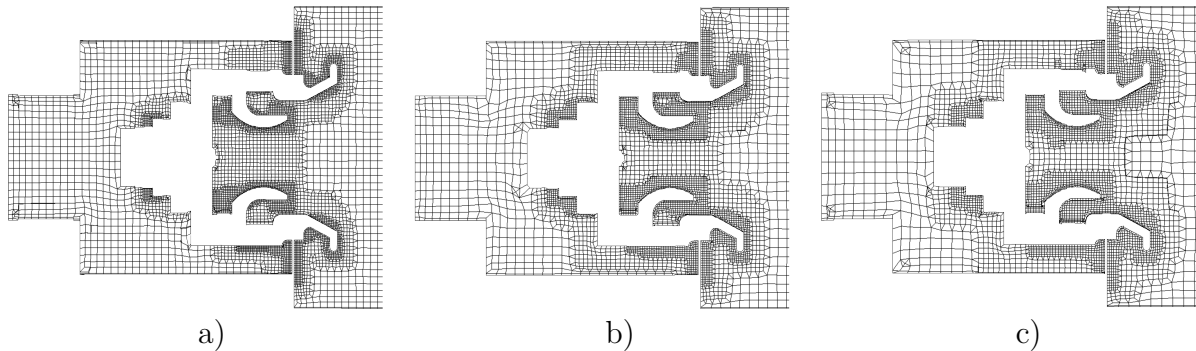
Figure 3.3: Control volume distribution around the swirler; a) coarse, b) medium, c) fine

3.2.   Boundary and Initial Conditions

On two ends of the combustor, as shown in Figure 3.4, air inlet and outlet boundary selections were defined. Adiabatic boundary condition was set for the chamber wall selection. The air and fuel introduction were prescribed with constant mass flows of 0.8 kg/s and 0.023 kg/s, and temperatures of 650 K and 300 K respectively. The outlet section was defined with a constant pressure of 9.12 bar. Table 3.2 specifies used boundary conditions.

Table 3.2: Boundary conditions

Air mass flow	0.8 kg/s
Air temperature	650 K
Fuel mass flow	0.023 kg/s
Fuel temperature	300 K
Walls	Adiabatic BC (heat flux 0 W/m^2)
Outlet pressure	9.12 bar
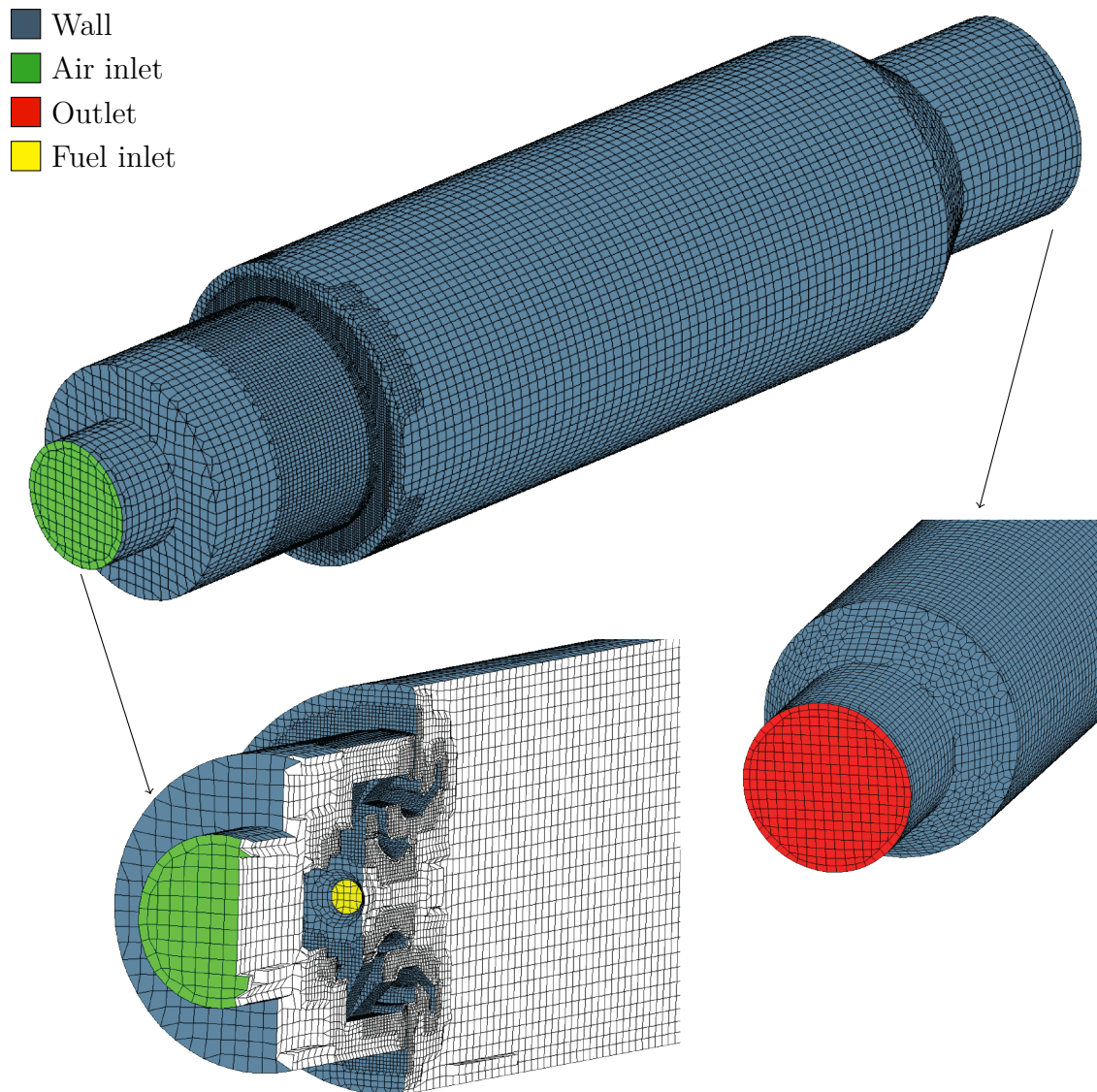
Figure 3.4: Boundary selections

The initial conditions are shown in Table 3.3. The air was prescribed as quiescent, with the pressure equal to the outlet and the temperature of 650 K. The air density was calculated according to the ideal gas law. AVL FIRE™ default values for the turbulent length scale and kinetic energy were used, 0.001 m and 0.001 m^2s^{-2} respectively [30].

Table 3.3: Initial conditions

Pressure	9.12 bar
Temperature	650 K
Turbulent length scale	0.001 m
Turbulent kinetic energy	0.001 m^{2}s^{-2}

3.3.   Spray Setup

The Lagrangian spray requires a definition of the spray angle, according to Figure 3.5. The half outer cone angle δ_2 was set to 22°, and the half inner cone angle δ_1 was defined as 2°, totaling the spray angle at 20°. The Start of Injection (SOI) was set at 2 ms from the simulation start. The spray nozzle location, i.e., particle introduction location, was defined with coordinates of the nozzle exit plane center, which was set to 0.062 m alongside the axial axis.
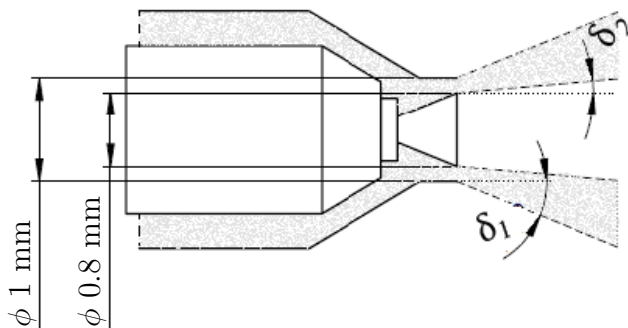
Figure 3.5: Fuel nozzle schematics

The maximum parcel size on the fuel inlet was set to 150 μm and the total of 27 parcels, detailed in Table 3.4, were being injected into the domain each time step. Number of introduced particles equals the product of individual components in the table.

Table 3.4: Particle introduction from the nozzle

Number of different particle sizes introduced per time step and radius	3
Number of radial parcels release location on nozzle hole	3
Number of circular parcels release location on each radial parcel	3

Employed spray submodels, described in Section 2.3.1., are given in Table 3.5.

Table 3.5: Spray submodels

Drag law model	Schiller-Naumann
Turbulent dispersion model	Enable [30]
Evaporation model	Abramzon-Sirignano
Breakup model	WAVE
Trubulence model	k-ζ-f

3.4.   Combustion Setup

The combustion process was initiated by introducing energy into eight evenly distributed points 100 mm from the fuel inlet, simulating spark plugs. Spark plugs were charged at 0.0031 s of simulation time. To model the combustion process two chemistry solution methods were employed:

1. General Gas Phase Reactions (GGPR) - JP-10 reaction mechanism, presented in Section 2.4.2., was assembled for FIRE internal chemistry interpreter. FIRE internal chemistry interpreter evaluates reaction rates depending on species concentrations and temperature, enabling direct coupling of the gas phase kinetics in a 3D CFD calculation [30].

2. AVL TABKIN™ Flamelet Generated Manifold (FGM), referred to as TABKIN henceforth - the look-up tables of the JP-10 reaction mechanism were created using the TABKIN Table Generation Tool.

Table 3.6 shows the data used for the spark ignition. The energy factor is a model parameter which defines the intensity of the spark event. Larger values lead to faster local temperature increase.

Table 3.6: Spark ignition setup

Spark timing	0.0031 s
Flame kernel size	0.008 m
Ignition duration	0.0015 s
Energy factor	10 (GGPR); 20 (TABKIN)

3.5.   Simulation Setup

Numerical simulations were solved as transient and weakly compressible. SIMPLE algorithm was used for the pressure-velocity coupling. The time discretization was performed automatically, based on the Courant-Friedrichs-Lewy (CFL) number of the gas phase, with the upper threshold of 10. Minimum and maximum time steps were defined as $1 \cdot 10^{-7}$ and $1 \cdot 10^{-5}$. The continuity equation was discretized using the Central Differencing Scheme (CDS) and the momentum equations were discretized using the combination of CDS and Upwind Differencing Scheme (UDS) with a blending factor of 0.5. Turbulence and energy equations were discretized by employing UDS. Furthermore, convergence criteria for the momentum and energy were set to 10^{-4} and to 10^{-5} for the pressure. Lastly, underrelaxation factors were employed as follows: 0.5 for the pressure, 0.6 for the momentum and 0.8 for the energy.

4 | Results

This chapter starts with the mesh dependency test of computational domains presented in the previous chapter. Further, the results of spray development, temperature and pressure distributions as well as the flame formation of both GGPR and FGM models are shown.

4.1. Mesh Dependency

Velocity and streamline distribution as well as the temperature around the swirler were analyzed for the mesh dependency. Figures 4.1 and 4.2 show velocity and temperature fields close to swirler at 2 ms, respectively. The left side of mentioned figures shows the plane along the axial axis, whereas the right side portrays cross sections located 0.1 m from the air inlet. Looking at the results, no considerable discrepancies among individual domains are visible.
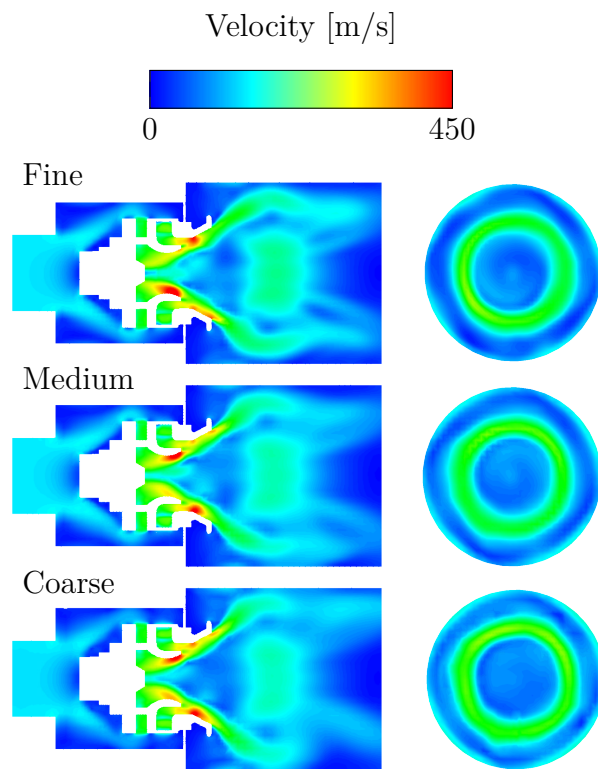
Velocity [m/s]

Figure 4.1: Mesh dependency of the velocity field at SOI
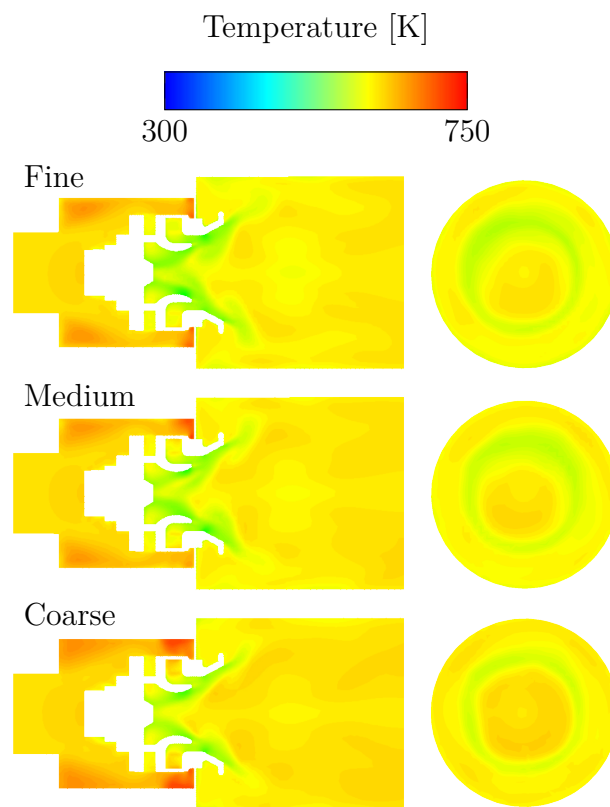
Temperature [K]

Figure 4.2: Mesh dependency of the temperature field at SOI

Figure 4.3 shows velocity and temperature profiles in the radial direction at the SOI, located at 0.1 mm from the air inlet. All three profiles exhibit similar behavior.
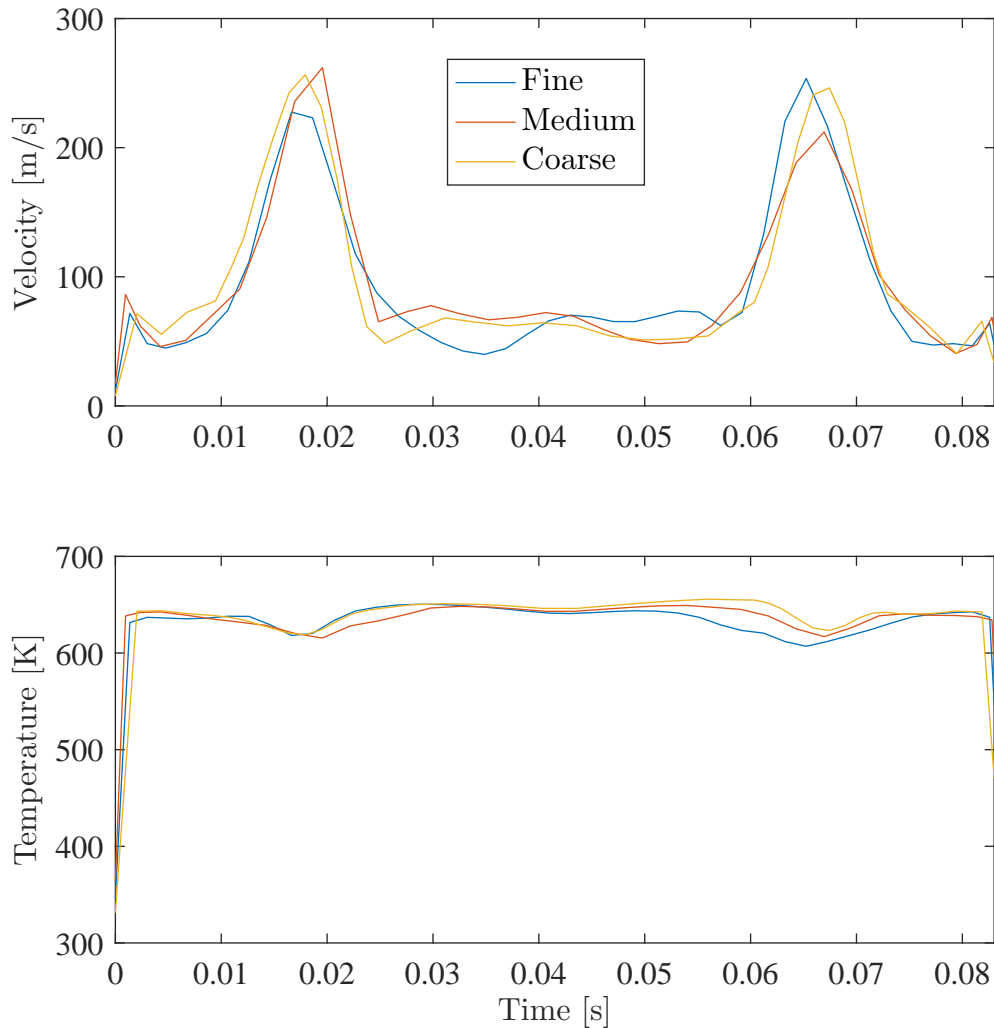
Figure 4.3: Mesh dependency of temperature and velocity at 100 mm from air inlet

In Figure 4.4, streamlines colored with the gas velocity are shown. It can be noticed that uniform swirl flow forms at the exit from the swirler, straightening towards the end of the combustor. All three computational meshes display similar behavior.

Velocity [m/s]

0   450

Fine

Medium
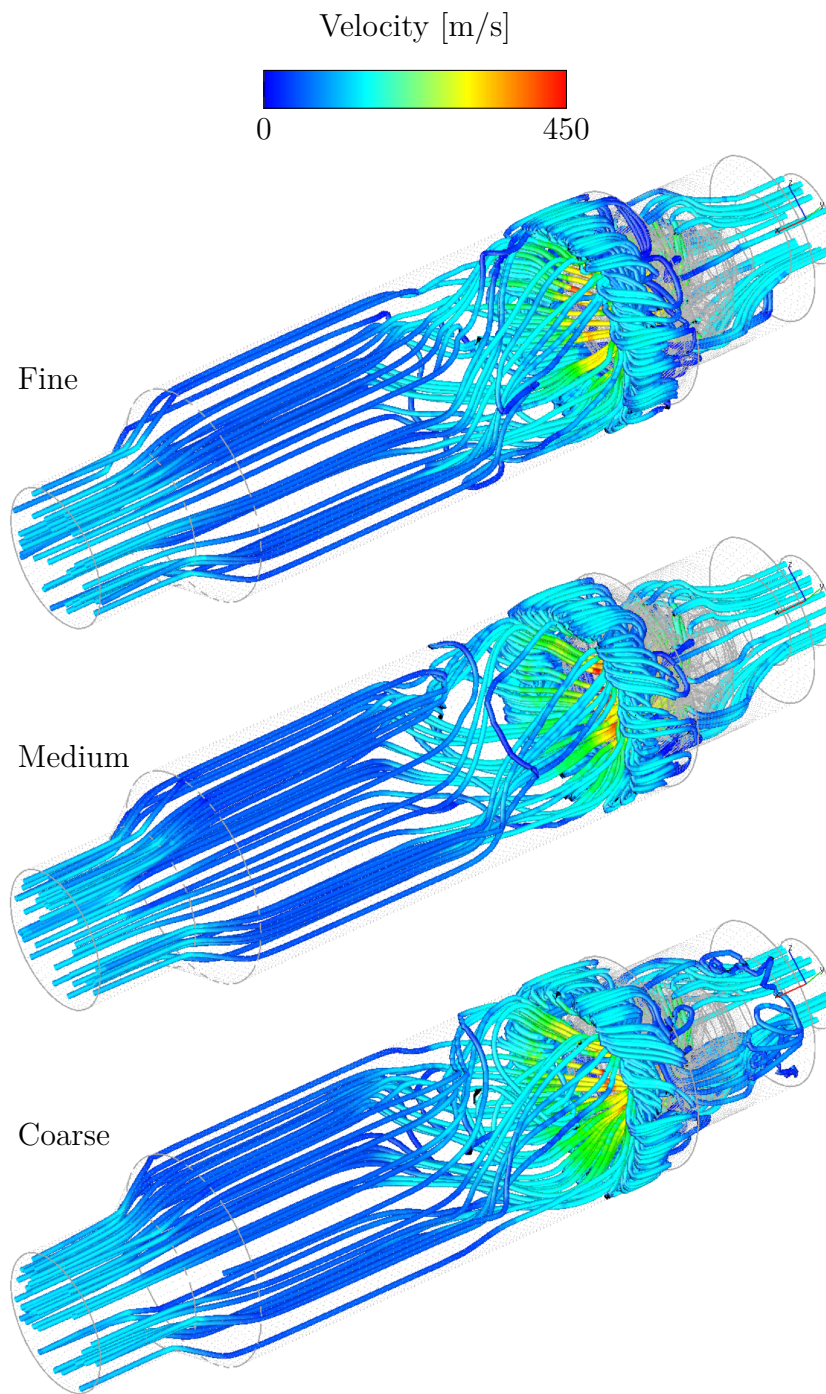
Coarse

Figure 4.4: Mesh dependency of the velocity field, shown with streamlines, at SOI

Mesh dependency results exhibit similar values for velocity and temeprature fields of all computational meshes. It can be concluded that the coarse mesh is able of providing satisfactory results, hence it is used for all further computations.

4.2.   Spray Development

Start of the continuous injection is at 2 ms from the simulation start. Creation of the spray cone as well as the vapor cloud are shown in Figure 4.5. Liquid parcels are colored according to the provided scale. Correlating to the spray setup, the largest droplet diameter is equal to 150 μm close to the fuel injection point. Due to droplet atomization caused by aerodynamic forces, and evaporation caused by the stream of hot air, droplets decrease in size further down the chamber and eventually evaporate. Hollow-cone JP-10 vapor cloud, denoting the mass fraction of 0.05, is shown in the same figure with a transparent isosurface.
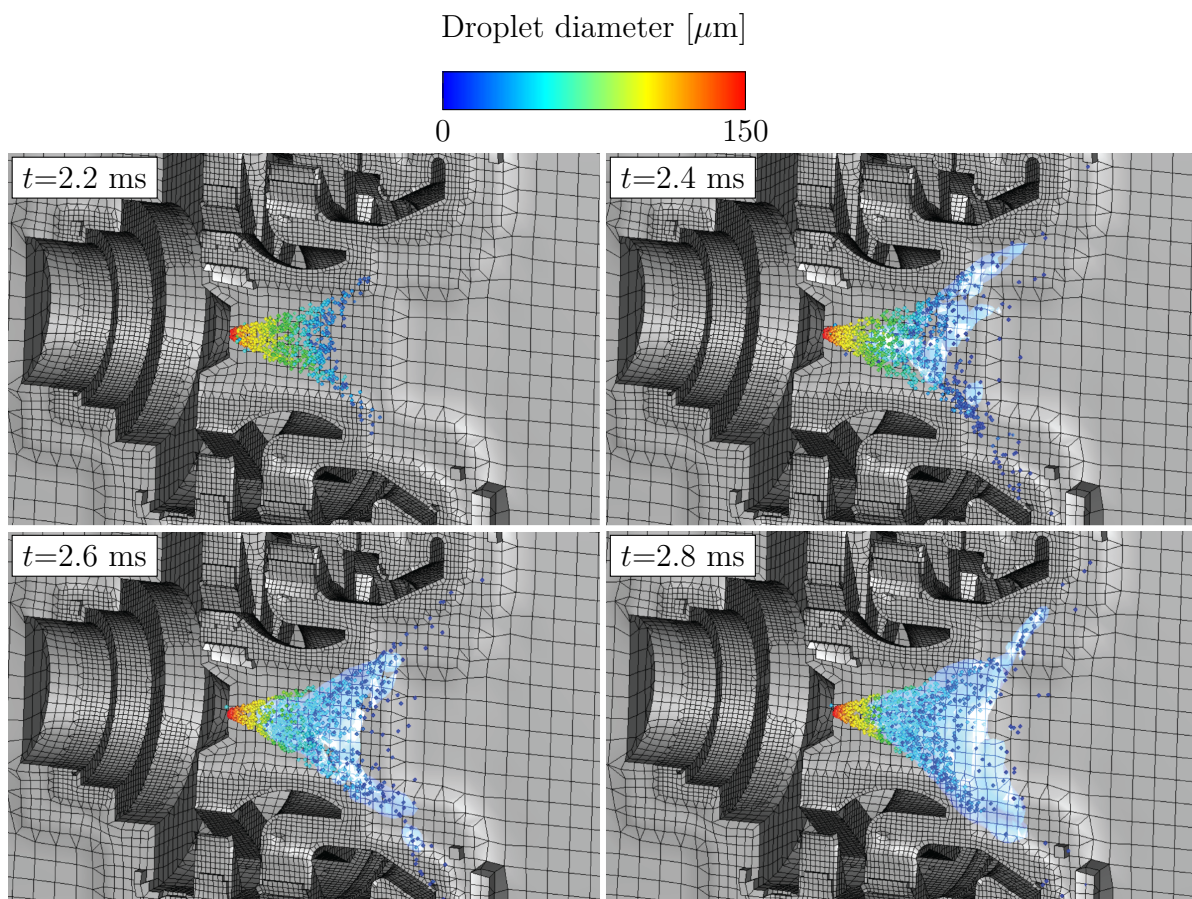
Figure 4.5: Spray development

Figure 4.6 shows curves of injected and evaporated fuel mass in relation to time. As seen in the fuel injection curve, the injected mass rises linearly, in accordance to 27 injected parcels each time step. The evaporated fuel mass curve follows closely, with a short spray forming delay observed at SOI, which is in conjunction with Figure 4.5. The total amount of injected fuel from SOI to 12 ms of simulation time is around 0.2 g.
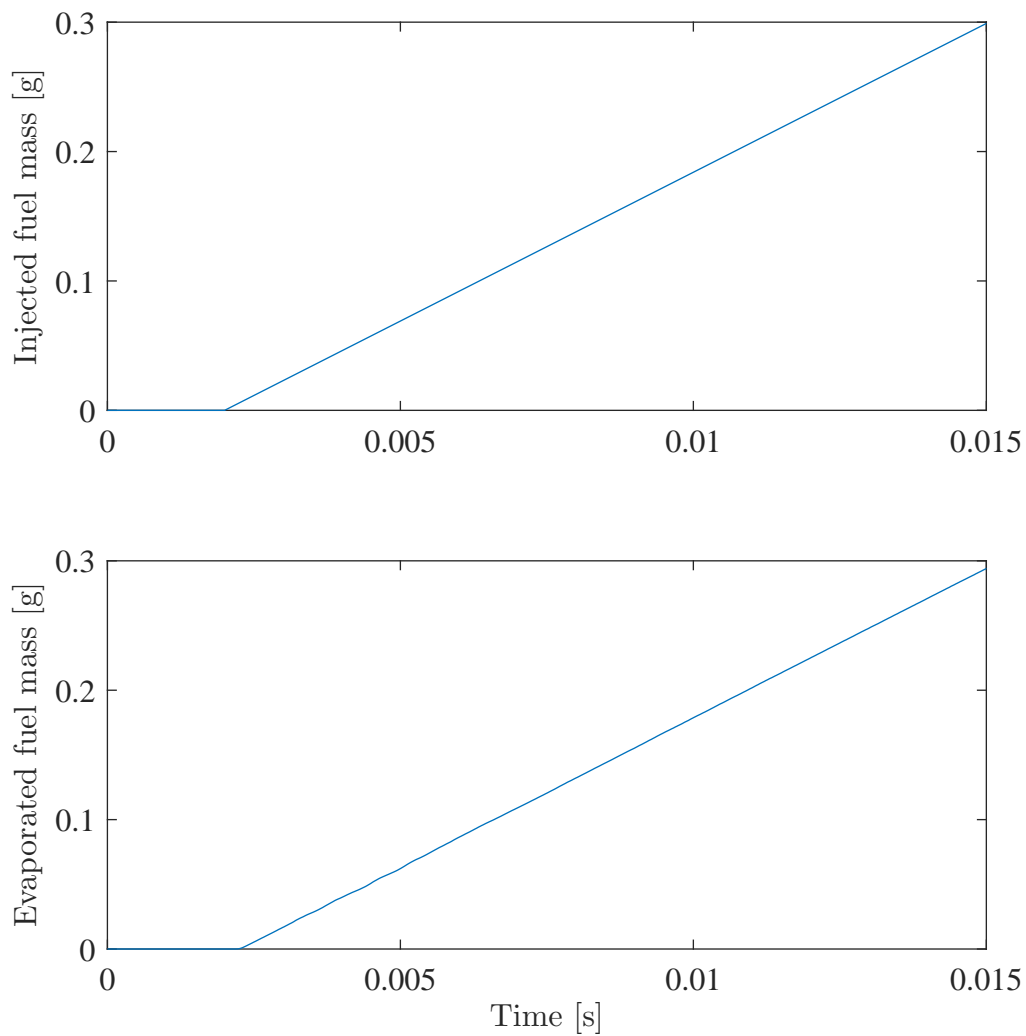
Figure 4.6: Injected and evaporated fuel mass

4.3.   Ignition and Combustion

The ignition starts at 3.1 ms from the simulation start, or 1.1 ms from the SOI. Throughout the single phase flow as well as the spray process, up until the ignition point, both GGPR and TABKIN simulations are identical to another. The left side of Figure 4.7 shows the temperature field development during combustion for GGPR, while the right side represents results of the TABKIN modeling approach.

The first illustration of the series, providing results at 3.2 ms, shows larger flame kernels in TABKIN, merely due to bigger energy factor. At the same time, the flame propagation is faster with GGPR (observed in times from 3.2 ms to 4.2 ms). This can also be seen in Figure 4.8, where GGPR curve of mean temperature rises steeper. The source of differences in the mean temperature profiles and flame development is in different spark energy definitions. In the GGPR combustion, the source calculated from the spark are enhanced by the energy factor and introduced into the enthalpy equation leading to higher temperatures of the computational volumes covered by the flame kernel. On the other hand, tabulation chemistry uses progress variable (pV) source deposit in order to ignite the mixture. This means that pV equation source term is set in a way, so that pV reaches 1.0 instantaneously in the spark region, during the spark event. Therefore, no extra energy is deposited, and spark temperature is lower when compared to the GGPR setup, leading to a slower (gentler slope of the temperature curve) combustion.
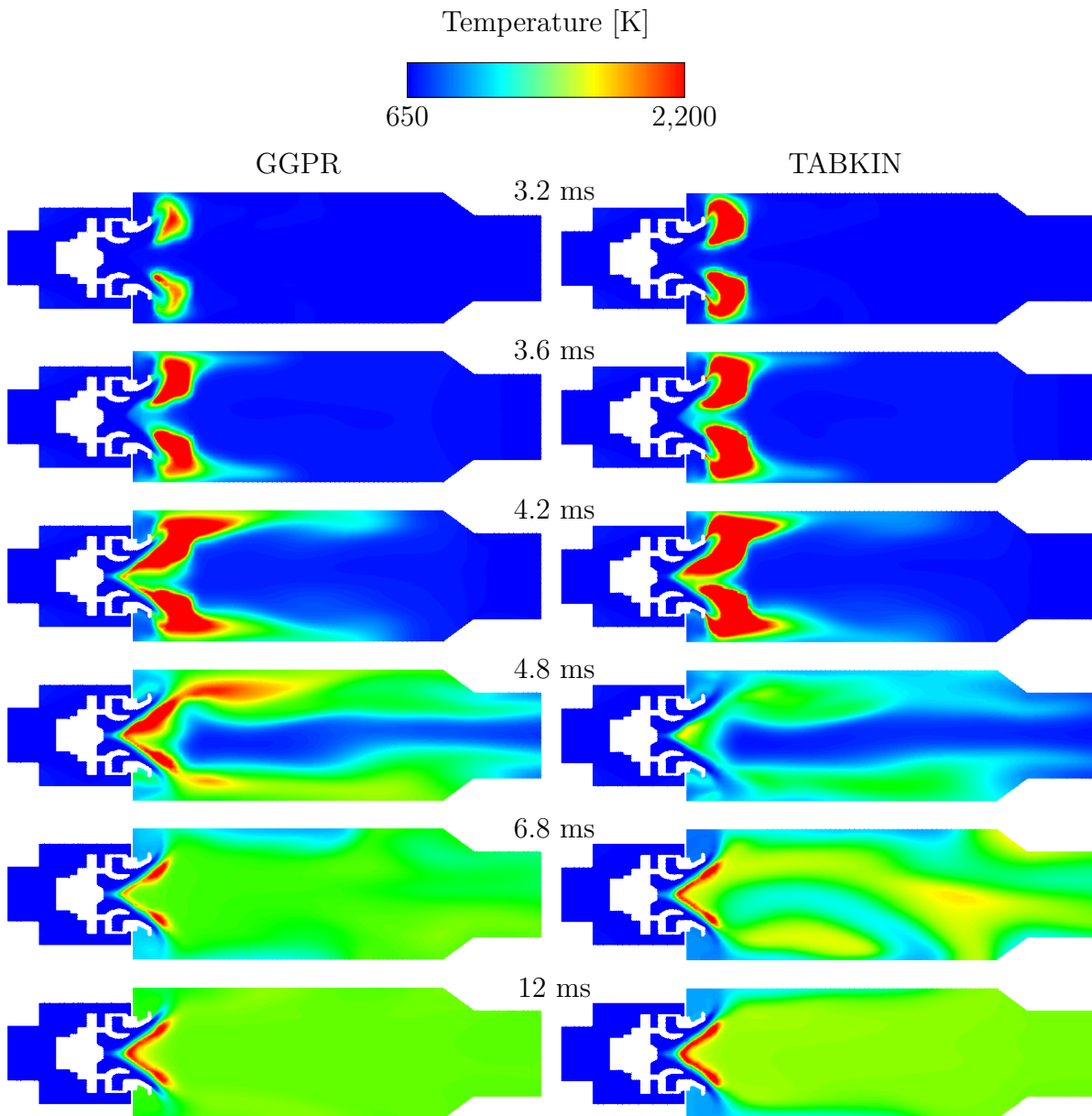
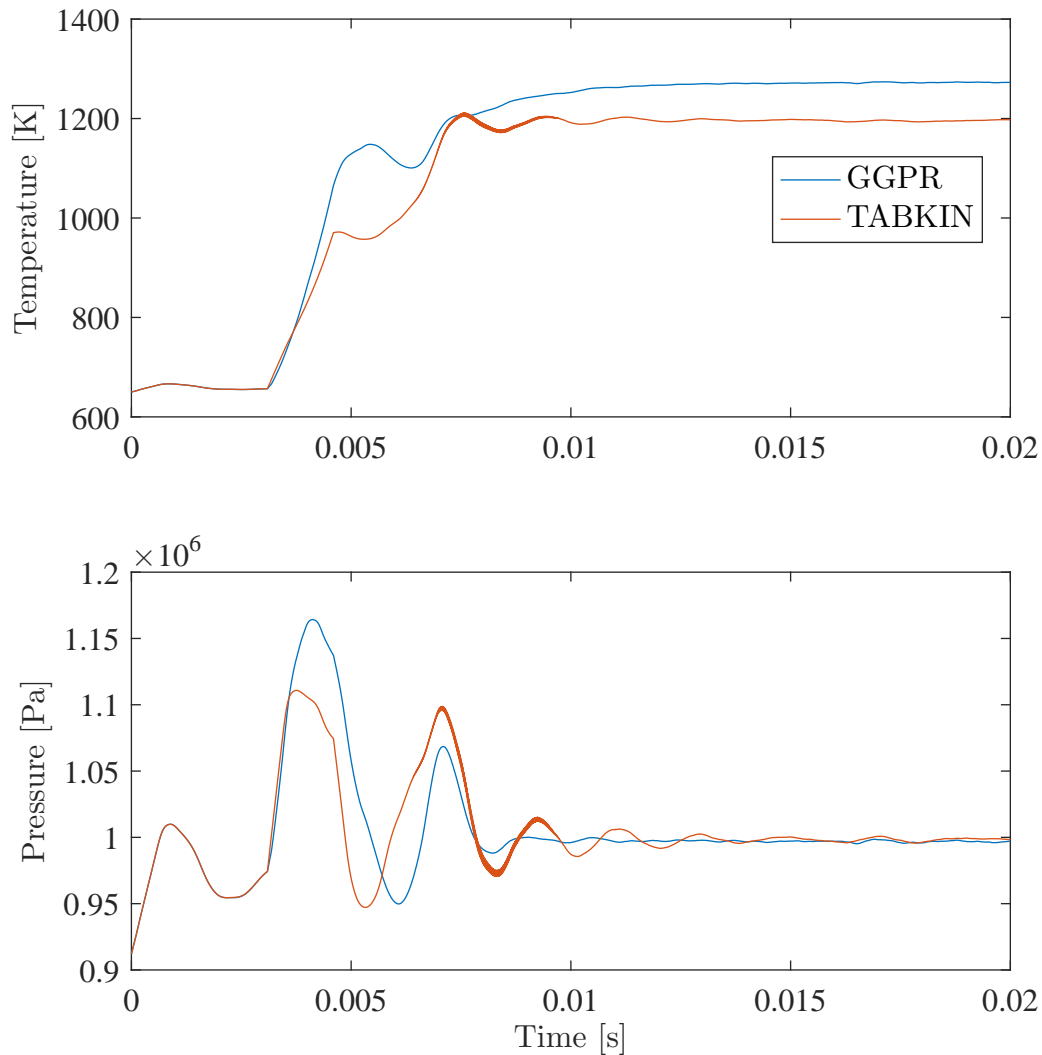Figure 4.7: Comparison of temperature fields during ignition and combustion

Figure 4.8: Mean tempearture and pressure change

As seen in Figure 4.8, oscillations in mean temperature lessens at around 8 ms, ultimately leading to quasi stationary state (Figure 4.7, last illustration) at around 12 ms. Some differences in stationary mean temperatures are observed, specifically 1267 K for GGPR versus 1198 K for TABKIN. Mean pressures of both approaches are nearly identical, with GGPR experiencing higher peak during the flame formation phase.

Differences in temperatures along the centerline at quasi stationary state, starting with the fuel nozzle exit, can be seen in Figure 4.9. Good matching of the results can be observed, especially in the primary zone where temperatures are identical. TABKIN yields slightly higher temperatures in the secondary zone. This indicates that TABKIN

is experiencing larger temperature drops along the radial axis in the secondary zone, as GGPR provides higher mean temperature.
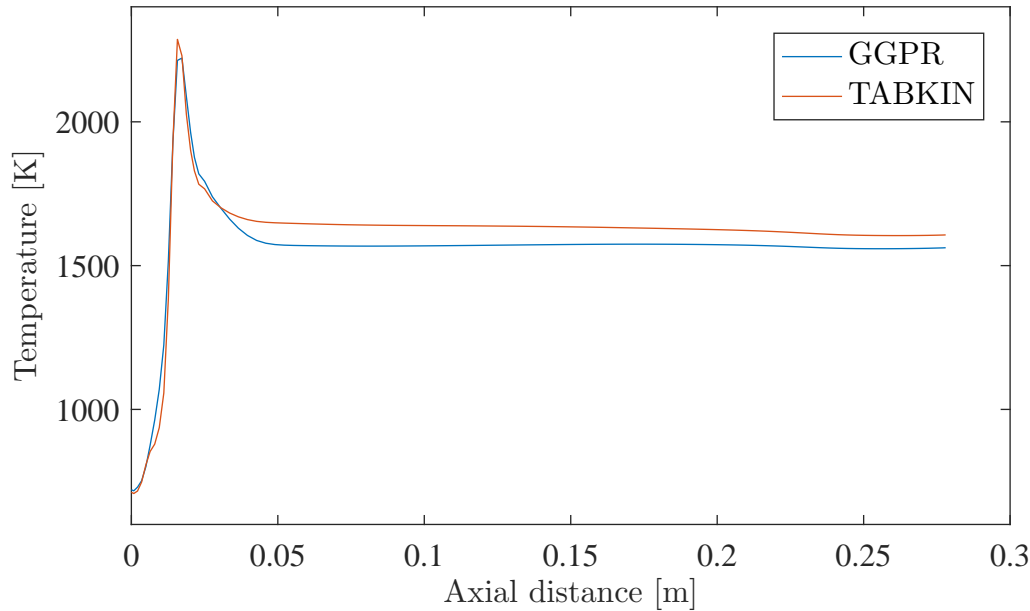
Figure 4.9: Temperature change along the centerline

It is worth mentioning that the amount of energy introduced by spark doesn't affect the final steady state temperature of both modeling approaches, as long as that energy is large enough to ignite the fuel. This is shown in Figure 4.10, where mean temperature curves of the TABKIN approach are presented for energy factors of 20, 50 and 150. Larger energy factors are expected to deliver higher temperature peaks in the early stages of combustion. Accordingly, energy factor 20 exhibits gradual rise to the quasi stationary temperature, whereas energy factors 50 and 150 peak at around 1600 K and 3600 K respectively, before converging to the stationary temperature.
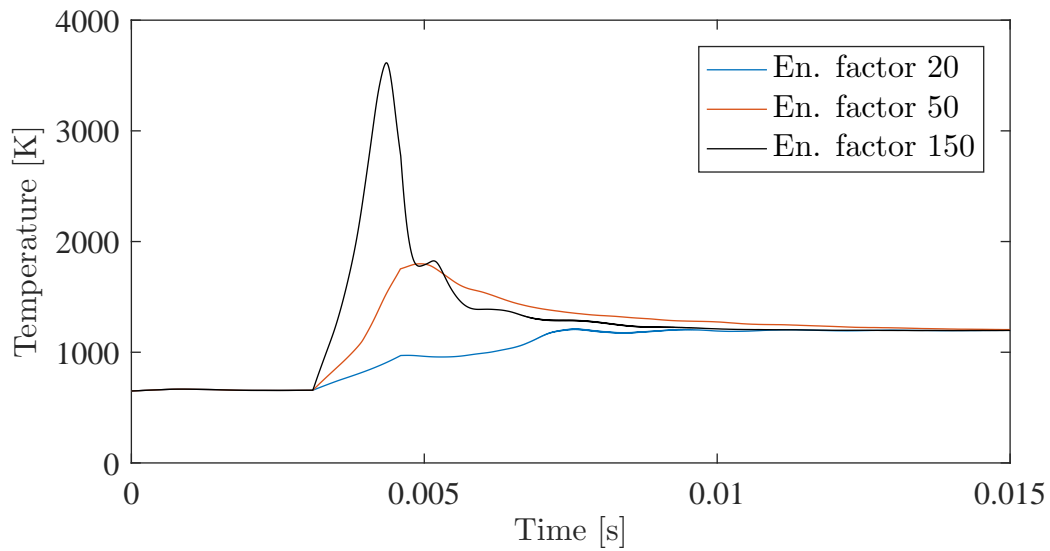
Figure 4.10: Mean tempearture curve for different energy factors (TABKIN)

Figure 4.11 shows temperature fields of certain cross sections. Numbers in the middle represent the distance from the air inlet. The smaller cross section at 80 mm from the air inlet displays the primary zone of combustion in between the stages of the swirler. Temperature fields in the primary zone (the first two illustrations) are showing satisfactory congruence. In the secondary zone, some discrepancies between approaches are noticeable, with TABKIN experiencing larger temperature drops. This goes hand in hand with conclusions drawn from Figures 4.8 and 4.9.
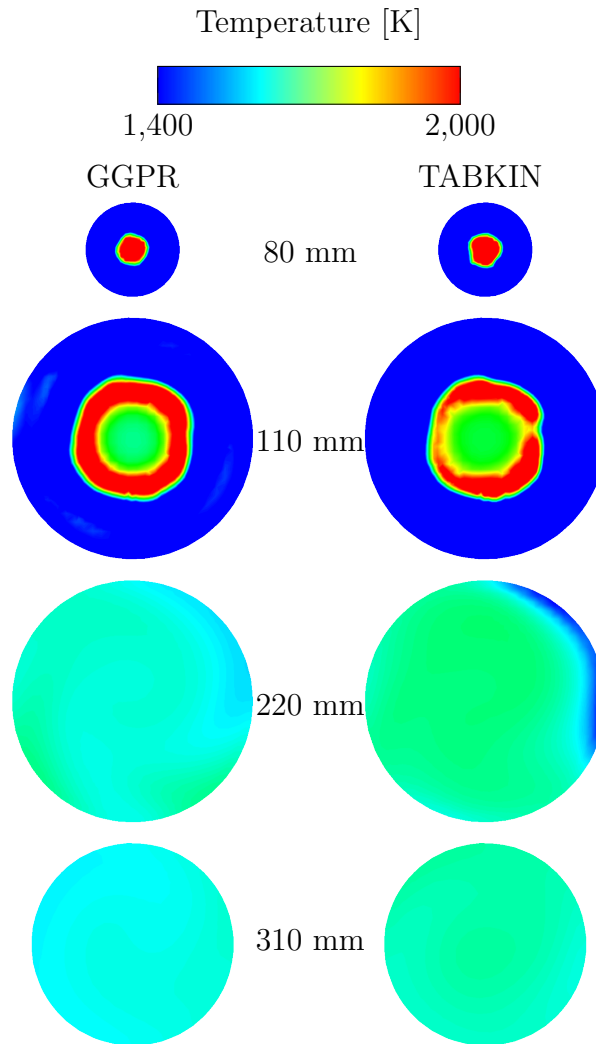
Figure 4.11: Cross section temperature fields at the quasi stationary state

4.4.   Data Comparison

Comparisons of turnaround times as well as differences in results are given below. Computational simulations were conducted on two Intel® Xeon® E5645 processors using 11 cores. Table 4.1 provides information on computational times from simulation start to 11 ms.

Table 4.1: Computational times at t=11 ms

GGPR [hh:mm:ss]	TABKIN [hh:mm:ss]	Reduction factor
73:01:02	13:10:03	5.55

As it can be seen from the table, reduction in computational times is substantional - roughly 5.5 times. This turnaround acceleration comes with a penalty of 5.5% mean temperature decrease of TABKIN in comparison to GGPR in quasi stationary state, as shown in Table 4.2. Differences in pressures are practically negligible.

Table 4.2: Mean temperatures and pressures at t=11 ms

	Mean temperature	Mean pressure
GGPR	1267 K	997397 Pa
TABKIN	1198 K	998271 Pa
Difference	5.5%	0.09%

5 | Conclusion

In this thesis, the feasibility analysis of TABKIN™ FGM model with an application in the jet engine combustion chamber was conducted. TABKIN™ results were compared to validated and accurate, albeit computationally demanding GGPR modeling approach. Relatively simple detailed chemical kinetic mechanism, consisted of 174 elementary steps among 36 species, of a military-grade high-density fuel JP-10 was employed. In the first step, the most appropriate computational domain was determined by performing mesh dependency tests of temperature and velocity fields. Spray formation and development as well as fuel evaporation were analyzed. Furthermore, formation of high temperature regions was shown, with the simulation reaching quasi-stationary state at around 12 ms of simulation time. It was addressed that the fuel ignition behaves differently between respective chemistry modeling approaches due to different energy introductions through sparks.

The FGM model provides satisfying predictive capabilities in comparison to GGPR. Temperatures in the primary zone are very similar, while some discrepancies are visible further away from the swirler. Differences in mean temperatures are 5.5% and differences in pressures are negligible. On the other hand, the decrease in turnaround time is significant, measured 5.5 times at 11 ms of simulation time.

It is important to address that GGPR is only as good as the detailed chemical kinetics mechanism describing the chemical process. Obtained results show correct physical and chemical behavior. Further work on the subject could involve more detailed chemical mechanism including hydrocarbon mixtures such as kerosene type fuels. Additionally, further work could include simulations of more complex and/or actual combustion chambers used in industry, with secondary airflow entering the chamber through the liner.

Bibliography

[1] Sforza, P.M.. Theory of Aerospace Propulsion. 2nd ed.; Butterworth-Heinemann; 2016.

[2] The Jet Engine. 5. ed.; Rolls Royce plc; 1996.

[3] Westbrook, C.K., Pitz, W.J., Herbinet, O., Curran, H.J., Silke, E.J.. A comprehensive detailed chemical kinetic reaction mechanism for combustion of n-alkane hydrocarbons from n-octane to n-hexadecane. Combustion and Flame 2009;156(1):181–199. doi:10.1016/j.combustflame.2008.07.014.

[4] Hemighaus, G., Bacha, J., Barnes, F., Franklin, M., Gibbs, L., Hogue, N., et al. Aviation Fuels Technical Review. Tech. Rep.; Chevron Corporation; 2007.

[5] Edwards, T., Maurice, L.Q.. Surrogate Mixtures to Represent Complex Aviation and Rocket Fuels. Journal of Propulsion and Power 2001;17(2):461–466. doi:10.2514/2.5765.

[6] Edwards, T.. Liquid Fuels and Propellants for Aerospace Propulsion: 1903-2003. Journal of Propulsion and Power 2003;19(6):1089–1107. doi:10.2514/2.6946.

[7] Hank, J., Murphy, J., Mutzman, R.. The X-51A Scramjet Engine Flight Demonstration Program. In: 15th AIAA International Space Planes and Hypersonic Systems and Technologies Conference. 2008,doi:10.2514/6.2008-2540.

[8] Burdette, G.W., Lander, H.R., McCoy, J.R.. High-energy fuels for cruise missiles. Journal of Energy 1978;2(5):289–292.

[9] Kandaramath Hari, T., Yaakob, Z., Binitha, N.N.. Aviation biofuel from renew-

able resources: Routes, opportunities and challenges. Renewable and Sustainable Energy Reviews 2015;42:1234–1244. doi:10.1016/j.rser.2014.10.095.

[10] Gegg, P., Budd, L., Ison, S.. The market development of aviation biofuel: Drivers and constraints. Journal of Air Transport Management 2014;39:34–40. doi:10.1016/j.jairtraman.2014.03.003.

[11] Yilmaz, N., Atmanli, A.. Sustainable alternative fuels in aviation. Energy 2017;140:1378–1386. doi:10.1016/j.energy.2017.07.077. arXiv:arXiv:1011.1669v3.

[12] Petranović, Z., Vujanović, M., Duić, N.. Towards a more sustainable transport sector by numerically simulating fuel spray and pollutant formation in diesel engines. Journal of Cleaner Production 2015;88:272–279. doi:10.1016/j.jclepro.2014.09.004.

[13] Petranović, Z.. Numerical modelling of spray and combustion processes using the Euler Eulerian multiphase approach. Ph.D. thesis; University of Zagreb, Faculty of Mechanical Engineering and Naval Arhitecture; 2016.

[14] Vujanović, M., Petranović, Z., Edelbauer, W., Duić, N.. Modelling spray and combustion processes in diesel engine by using the coupled Eulerian–Eulerian and Eulerian–Lagrangian method. Energy Conversion and Management 2016;125:15–25. doi:10.1016/j.enconman.2016.03.072.

[15] Warnatz, J., Maas, U., Dibble, R.W.. Combustion: Physical and chemical fundamentals, modeling and simulation, experiments, pollutant formation. 2006.

[16] Li, S.C., Varatharajan, B., Williams, F.A.. Chemistry of JP-10 Ignition. AIAA Journal 2001;39(12):2351–2356. doi:10.2514/2.1241.

[17] Lindstedt, R., Markaki, V.. Detailed and Simplified Chemical Kinetics of Aviation Fuels and Surrogates. Tech. Rep. Final Report on Grant FA8655-06-1-3052; 2009.

[18] Dooley, S., Won, S.H., Chaos, M., Heyne, J., Ju, Y., Dryer, F.L., et al. A jet fuel surrogate formulated by real fuel properties. Combustion and Flame 2010;157(12):2333–2339. doi:10.1016/j.combustflame.2010.07.001.

[19] Dagaut, P., Cathonnet, M.. The ignition, oxidation, and combustion of kerosene: A review of experimental and kinetic modeling. Progress in Energy and Combustion Science 2006;32(1):48–92. doi:`10.1016/j.pecs.2005.10.003`.

[20] Edwards, T., Colket, M., Cernansky, N., Dryer, F., Egolfopoulos, F., Friend, D., et al. Development of an Experimental Database and Kinetic Models for Surrogate Jet Fuels. In: 45th AIAA Aerospace Sciences Meeting and Exhibit. 2007,doi:`10.2514/6.2007-770`.

[21] Vujanović, M.. Numerical Modelling of Multiphase Flow in Combustion of Liquid Fuel. Ph.D. thesis; University of Zagreb, Faculty of Mechanical Engineering and Naval Architecture; 2010.

[22] Kong, S.C., Marriott, C.D., Reitz, R.D., Christensen, M.. Modeling and Experiments of HCCI Engine Combustion Using Detailed Chemical Kinetics with Multidimensional CFD. SAE Technical Paper 2001;2011-01-10. doi:`10.4271/2001-01-1026`.

[23] Pope, S.B.. PDF methods for turbulent reactive flows. Progress in Energy and Combustion Science 1985;11(2):119–192. doi:`10.1016/0360-1285(85)90002-4`.

[24] Honnet, S., Seshadri, K., Niemann, U., Peters, N.. A surrogate fuel for kerosene. Proceedings of the Combustion Institute 2009;32 I:485–492. doi:`10.1016/j.proci.2008.06.218`.

[25] Montgomery, C.J., Cannon, S.M., Mawid, M.a.. Reduced Chemical Kinetic Mechanisms for JP-8. American Institute of Aeronautics and Astronautics 2002;(January):Paper 2002–0336. doi:`10.2514/6.2002-336`.

[26] Luche, J., Reuillon, M., Boettner, J.C., Cathonnet, M.. Reduction of Large Detailed Kinetic Mechanisms: Application to Kerosene/Air Combustion. Combustion Science and Technology 2004;176(11):1935–1963. doi:`10.1080/00102200490504571`.

[27] van Oijen, J.V., de Goey, L.. Modelling of Premixed Laminar Flames using Flamelet-Generated Manifolds. Combustion Science and Technology 2000;161(1):113–137. doi:`10.1080/00102200008935814`.

[28] Moukalled, F., Mangani, L., Darwish, M.. The Finite Volume Method in Computational Fluid Dynamics. Springer; 2016.

[29] Muller, P.. Glossary of terms used in physical organic chemistry (IUPAC Recommendations 1994). Pure and Applied Chemistry 1994;66(5):1077–1184. doi:10.1351/pac199466051077.

[30] AVL Fire Documentation, v2017. 2017.

[31] Tennekes, H.. A First Course in Turbulence. MIT Press; 1972.

[32] Zhiyin, Y.. Large-eddy simulation: Past, present and the future. Chinese Journal of Aeronautics 2015;28(1):11–24. doi:10.1016/J.CJA.2014.12.007.

[33] Hanjalić, K., Popovac, M., Hadžiabdić, M.. A robust near-wall elliptic-relaxation eddy-viscosity turbulence model for CFD. International Journal of Heat and Fluid Flow 2004;25(6):1047–1051. doi:10.1016/J.IJHEATFLUIDFLOW.2004.07.005.

[34] Durbin, P.A.. Near-wall turbulence closure modeling without "damping functions". Theoretical and Computational Fluid Dynamics 1991;3(1):1–13. doi:10.1007/bf00271513.

[35] Brennen, C.E.. Fundamentals of multiphase flow. Cambridge University Press; 2005.

[36] Kadocsa, A.. Modeling of Spray Formation in Diesel Engines. Ph.D. thesis; Budapest University of Technology and Economics; 2007.

[37] Reitz, R.D.. Modeling Atomization Processes in High-Pressure Vaporizing Sprays. Atomization and Sprays 1987;3:309–337.

[38] Abramzon, B., Sirignano, W.A.. Droplet vaporization model for spray combustion calculations. International Journal of Heat and Mass Transfer 1989;32(9):1605–1618. doi:10.1016/0017-9310(89)90043-4.

[39] Gosman, A.D., Loannides, E.. Aspects of Computer Simulation of Liquid-Fueled Combustors. Journal of Energy 1983;7(6):482–490. doi:10.2514/3.62687.

[40] Westbrook, C.K., Dryer, F.L.. Chemical kinetic modeling of hydrocarbon combustion. Progress in Energy and Combustion Science 1984;10(1):1–57. doi:10.1016/0360-1285(84)90118-7.

[41] Tap, F., Schapotschnikow, P.. Efficient Combustion Modeling Based on Tabkin CFD Look-up Tables: A Case Study of a Lifted Diesel Spray Flame. SAE Technical Paper 2012-01-0152 2012;doi:10.4271/2012-01-0152.

[42] Hajivand, M.. CFD Modeling of Kerosene Combustion With Various Initial Conditions and Fuel Droplet Diameters. NTU «KhPI» Bulletin: Series «Power and Heat Engineering Processes and Equipment» 2015;16:54–66.

[43] Cerinski, D.. Numerical Modelling of Spray and Combustion Processes in a Jet Engine Combustion Chamber. Master's thesis; University of Zagreb, Faculty of Mechanical Engineering and Naval Architecture; 2017.

A | Appendix

JP-10 decomposition

Table A.1: Irreversible reaction steps and associate rate parameters for ignition and combustion of JP-10 [16]

Number	Reaction	A	n	E_a
1	$C_{10}H_{16} \rightarrow C_2H_2 + 2C_2H_4 + C_4H_6$	5.00×10^{16}	0.0	85.4
2	$C_{10}H_{16} \rightarrow H + C_2H_4 + C_3H_3 + C_5H_8$	6.00×10^{16}	0.0	98.0
3	$C_{10}H_{16} \rightarrow H + C_2H_2 + C_3H_5 + C_5H_8$	6.00×10^{16}	0.0	98.0
4	$C_{10}H_{16} + O_2 \rightarrow HO_2 + C_2H_4 + C_3H_3 + C_5H_8$	3.98×10^{13}	0.0	50.9
5	$C_{10}H_{16} + O_2 \rightarrow HO_2 + C_2H_2 + C_3H_5 + C_5H_8$	7.92×10^{13}	0.0	47.6
6	$C_{10}H_{16} + OH \rightarrow H_2O + C_2H_4 + C_3H_3 + C_5H_8$	1.74×10^7	1.8	1.0
7	$C_{10}H_{16} + OH \rightarrow H_2O + C_2H_2 + C_3H_5 + C_5H_8$	3.80×10^6	2.0	−0.6
8	$C_{10}H_{16} + O \rightarrow OH + C_2H_4 + C_3H_3 + C_5H_8$	2.88×10^6	2.4	5.5
9	$C_{10}H_{16} + O \rightarrow OH + C_2H_2 + C_3H_5 + C_5H_8$	2.76×10^5	2.6	1.9
10	$C_{10}H_{16} + H \rightarrow H_2 + C_2H_4 + C_3H_3 + C_5H_8$	1.32×10^6	2.5	6.8
11	$C_{10}H_{16} + H \rightarrow H_2 + C_2H_2 + C_3H_5 + C_5H_8$	2.60×10^6	2.4	4.5
12	$C_{10}H_{16} + HO_2 \rightarrow H_2O_2 + C_2H_4 + C_3H_3 + C_5H_8$	4.76×10^4	2.5	16.5
13	$C_{10}H_{16}CHO_2 \rightarrow H_2O_2 + C_2H_2 + C_3H_5 + C_5H_8$	1.93×10^4	2.6	13.9
14	$C_5H_8 \rightarrow C_2H_4 + C_3H_4$	3.16×10^{12}	0.0	57.0
15	$C_5H_8 \rightarrow C_2H_3 + C_3H_5$	3.16×10^{12}	0.0	57.0
16	$C_5H_8 \rightarrow C_2H_2 + C_3H_6$	1.00×10^{16}	0.0	73.0
17	$C_5H_8 + O_2 \rightarrow HO_2 + C_2H_2 + C_3H_5$	3.00×10^{12}	0.0	0.0
18	$C_5H_8 + O_2 \rightarrow HO_2 + C_2H_3 + C_3H_4$	3.00×10^{12}	0.0	0.0

Continued on next page

Table A.1 – *cont'd*

Number	Reaction	A	n	E_a
19	$C_5H_8 + HO_2 \rightarrow H_2O_2 + C_2H_2 + C_3H_5$	1.00×10^{14}	0.0	0.0
20	$C_5H_8 + HO_2 \rightarrow H_2O_2 + C_2H_3 + C_3H_4$	1.00×10^{14}	0.0	0.0
21	$C_4H_6 \rightarrow 2C_2H_3$	1.80×10^{13}	0.0	85.1
22	$2C_2H_3 \rightarrow C_4H_6$	1.26×10^{13}	0.0	0.0
23	$C_3H_3 + CH_3 \rightarrow C_4H_6$	5.00×10^{12}	0.0	0.0
24	$C_4H_6 \rightarrow H + C_2H_2 + C_2H_3$	1.58×10^{16}	0.0	109.9
25	$C_4H_6 + OH \rightarrow CHO + H + C_3H_5$	5.00×10^{12}	0.0	0.0
26	$C_4H_6 + H \rightarrow H_2 + C_2H_2 + C_2H_3$	6.30×10^{10}	0.7	6.0
27	$C_4H_6 + H \rightarrow C_2H_3 + C_2H_4$	5.00×10^{11}	0.0	0.0
28	$C_4H_6 + CH_3 \rightarrow CH_4 + C_2H_2 + C_2H_3$	7.00×10^{13}	0.0	18.4